Supplementary Information

Observation of the crossover from quantum fluxoid to half quantum fluxoid in a chiral superconducting device

Masashi Tokuda[1*], Mai Nakao[1], Mori Watanabe[1], Sanghyun Lee[1], Ryoya Nakamura[1], Masaki Maeda[1], Nan Jiang[1, 2, 3], Di Yue[4, 5], Kazushi Aoyama[6], Takeshi Mizushima[7], Xiaofeng Jin[4, 5], Kensuke Kobayashi[8], and Yasuhiro Niimi[1, 2, 3**]

[1]Department of Physics, Graduate School of Science, Osaka University, Toyonaka, Osaka 560-0043, Japan.

[2]Center for Spintronics Research Network, Graduate School of Engineering Science, Osaka University, Toyonaka, Osaka 560-8531, Japan.

[3]Spintronics Research Network Division, Institute for Open and Transdisciplinary Research Initiatives, Osaka University, Suita, Osaka, 565-0871, Japan.

[4]State Key Laboratory of Surface Physics and Department of Physics, Fudan University, Shanghai 200433, People's Republic of China.

[5]Collaborative Innovation Center of Advanced Microstructures, Fudan University, Shanghai 200433, People's Republic of China.

[6]Department of Earth and Space Science, Graduate School of Science, Osaka University, Toyonaka, Osaka 560-0043, Japan.

[7]Department of Materials Engineering Science, Osaka University, Toyonaka, Osaka 560-8531, Japan.

[8]Institute for Physics of Intelligence, The University of Tokyo, Bunkyo-ku, Tokyo 113-0033, Japan.

*e-mail: tokuda@meso.phys.sci.osaka-u.ac.jp

**e-mail: niimi@phys.sci.osaka-u.ac.jp

Contents

1. Basic properties of Bi/Ni bilayer film	**3**
2. Current-voltage properties of ring-shaped Bi/Ni devices	**6**
3. How to analyze the LP oscillations	**8**
4. Reproducibility of the crossover in LP oscillations	**11**
5. Additional discussions on the crossover in LP oscillations	**16**
6. Upper critical field measurements in Bi/Ni bilayer film	**19**
7. Effect of spin-orbit coupling on the LP oscillation	**21**
8. Theoretical interpretation of the phase shift in LP oscillations	**25**

1. Basic properties of Bi/Ni bilayer film

In this work, we fabricated mesoscopic ring-shaped devices from a Bi/Ni bilayer film. Before the device fabrication, we measured the temperature dependence of resistance of Bi/Ni bilayer film using the ac lock-in technique. Four-terminal measurements were performed by directly attaching Al-Si (1%) bonding wires to the surface of the film, as shown in Fig. S1. The sample was cooled down from room temperature to about 2 K by using a ^{4}He flow refrigerator.

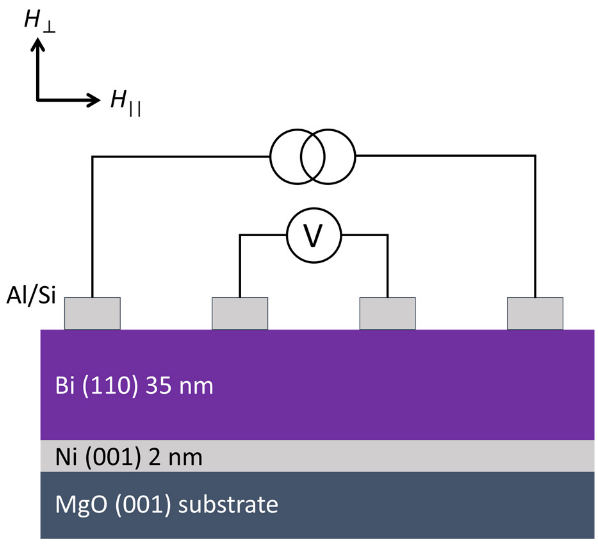

Fig. S1| Schematic image of the circuit to measure the resistance of Bi/Ni bilayer film with the four-terminal method. Al-Si (1%) wires were bonded at the surface of the Bi layer. The arrows indicate the directions of the external magnetic field.

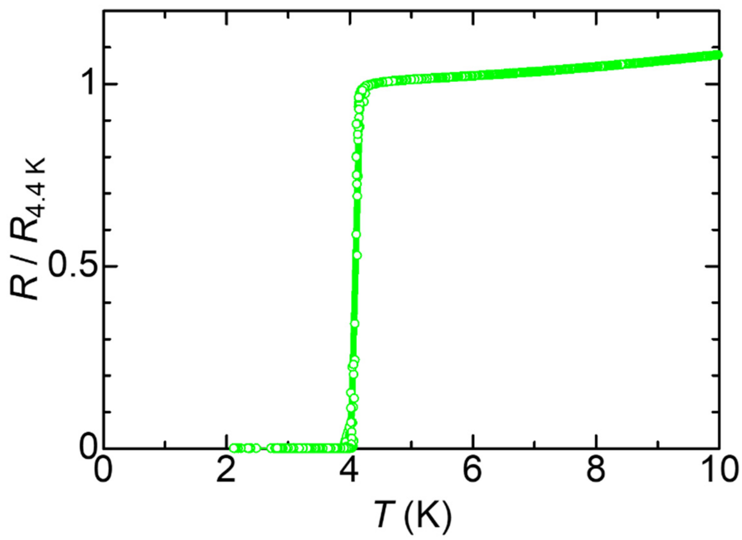

Fig. S2| Temperature dependence of R measured with the Bi/Ni bilayer film. The vertical axis is normalized by the resistance at 4.4 K just above the superconducting transition.

In Fig. S2, we show the temperature dependence of resistance R of the Bi/Ni bilayer normalized by R at $T = 4.4$ K just above the superconducting transition temperature $T_\mathrm{c} = 4.1$ K. In this work, T_c is defined as a temperature where R becomes a half value of $R_{4.4\ \mathrm{K}}$ at 4.4 K (normal state) at zero field. The superconducting transition temperature is consistent with that of a previous work[S1]. As mentioned in the main text, the Bi/Ni bilayer keeps good quality even after the device fabrication because T_c of the Bi/Ni film and that of the ring-shaped device are almost the same value.

Next, we measured Hall resistance with a Hall bar device fabricated with a Bi/Ni bilayer, in order to estimate the carrier density of Bi/Ni bilayer. The carrier density is used to calculate the penetration depth which is important for the device fabrication of ring-shaped devices, because the width of the ring must be wider than the penetration depth. Details of the calculation are described in the next paragraph. The measurement was performed at 10 K using the Hall bar device (see the inset of Fig. S3). The Hall resistance is shown in Fig. S3 where a small symmetric component has been subtracted from the raw data. From the slope of the Hall resistance, we estimated the carrier density as $n_\mathrm{c} = 4.9 \times 10^{22}$ cm^{-3} [S2]. Since the carrier densities of Bi and Ni are respectively 3×10^{17} cm^{-3} [S3] and 1.0×10^{23} cm^{-3} [S4], the present value is in between the carrier densities of Bi and Ni. The result indicates that the carrier in the Ni layer is doped into the Bi layer[11].

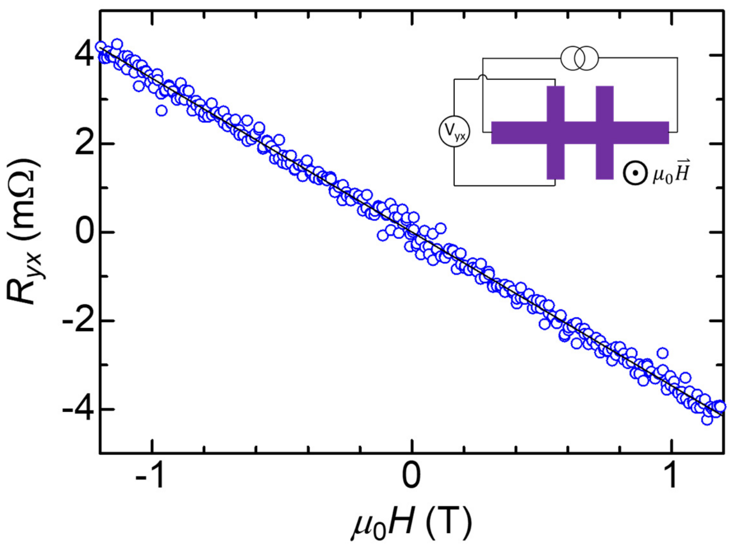

Fig. S3| Hall resistance measured at 10 K using a Hall bar device (the inset). The black solid line shows the liner fitting.

We then calculate the penetration depth of Bi/Ni. According to the two fluid model, the penetration depth is given as[S5]

$$\lambda = \sqrt{\frac{m^*}{\mu_0 n_\mathrm{s} e^{*2}}} \ , \tag{1}$$

where μ_0 is the permeability of vacuum, m^* is the effective mass, and e^* is the effective charge, i.e., $m^* = 2m_\mathrm{e}$ and $e^* = 2e$ (m_e is the mass of an electron and e is the elementary charge). The superfluid density n_s at 0 K is equal to the normal fluid density before the superconducting transition. By substituting the carrier density of the normal state for the superfluid density at 0 K, the penetration depth of Bi/Ni bilayer at 0 K is calculated as $\lambda = 17$ nm. The temperature dependence of λ can be expressed with the following formula[S5]:

$$\lambda(T) \approx \lambda(0)\left[1-\left(\frac{T}{T_\mathrm{c}}\right)^4\right]^{-1/2}, \tag{2}$$

and is illustrated in Fig. S4. The width of the ring-shaped device (≈ 500 nm) is much larger than the penetration depth at 2.5 K where the Little-Parks oscillations measurements were performed.

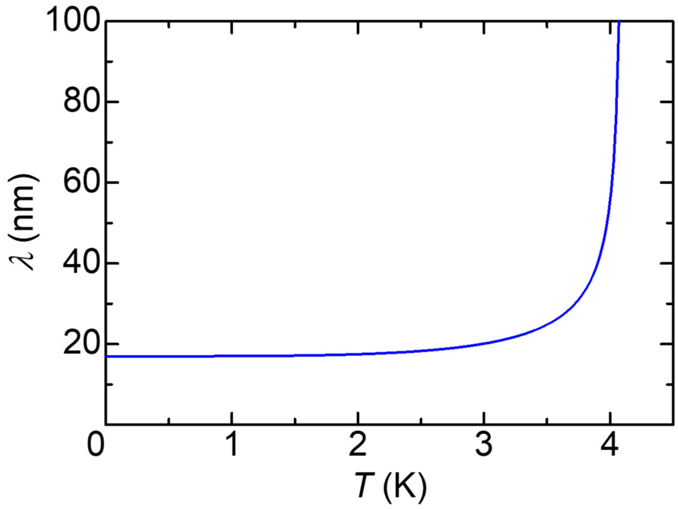

Fig. S4| Calculated temperature dependence of the penetration depth of Bi/Ni bilayer using Eq. (2). The penetration depth is about 18 nm at 2.5 K which is more than 20 times smaller than the width of the ring part.

2. Current-voltage properties of ring-shaped Bi/Ni devices

As mentioned in the main text, before measuring Little-Parks (LP) oscillations with Bi/Ni and Nb ring-shaped devices, we checked the dc current(I)-voltage(V) property of the devices, in order to obtain the critical current (I_c). Figure S5 shows a typical I-V curve obtained with a Bi/Ni ring-shaped device (sample #2) at 2.47 K. The voltage is zero up to $I_c = \pm 51$ μA.

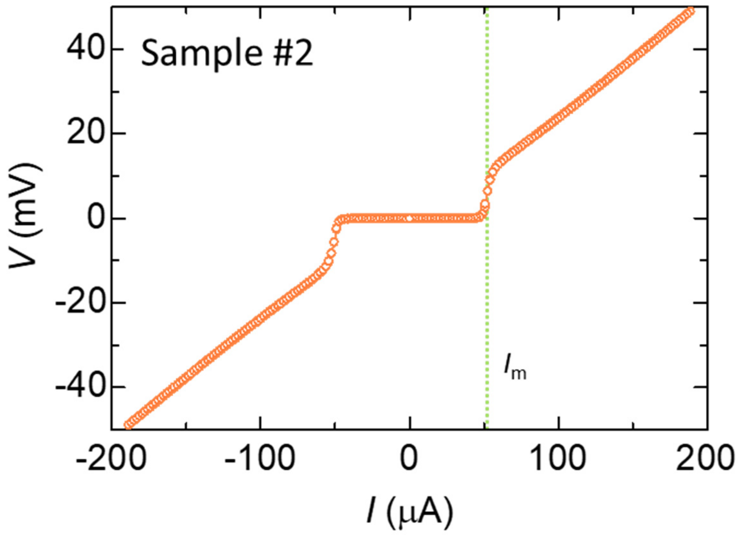

Fig. S5| Typical I-V curve of a Bi/Ni ring-shaped device measured with sample #2 at 2.47 K. The green dotted line indicates the measurement current I_m which corresponds to the current to measure the LP oscillations demonstrated in the main text.

We also measured I-V curves at different magnetic fields to see the oscillation of I_c. In Figs. S6a and S6b, we show the typical results obtained with other Bi/Ni ring-shaped devices (samples #3 and #4) at fixed temperatures (2.34 and 2.45 K, respectively). The magnetic field H was applied perpendicularly to the basal plane and normalized by $\mu_0 H_0 = \phi_0/S$ (~0.6 mT) where S is the surface of the ring. The critical current I_c takes maxima and minima at $H = nH_0$ and $H = (n + 1/2)H_0$, respectively. Such behavior can be seen in Figs. S6a and S6b. These results are consistent with the magnetic field dependence of resistance shown in Figs. S10-S13 as well as in Fig. 2b and Fig. 3 in the main text. As already discussed in Ref. S6, the oscillation of I_c at a fixed temperature is essentially the same as that of T_c.

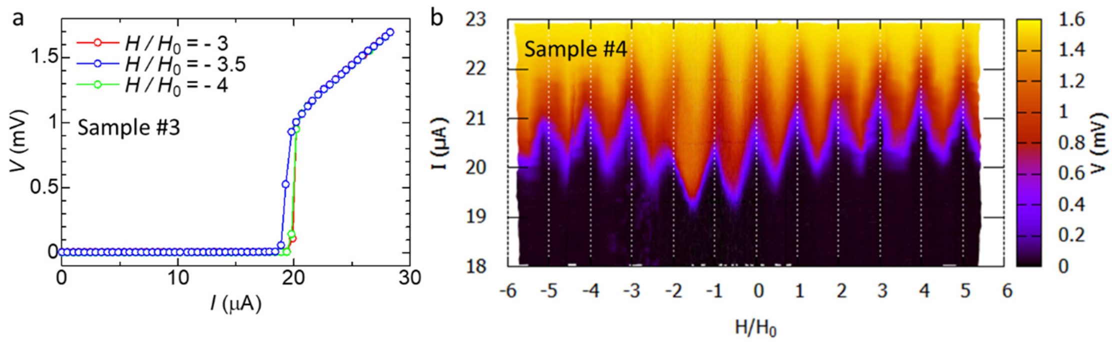

Fig. S6| I-V curves of Bi/Ni ring-shaped devises measured with (**a**) samples #3 and (**b**) sample #4. $\mu_0 H_0$ of samples #3 and #4 are 0.62 mT and 0.65 mT, respectively. The measurements were performed at 2.34 K for sample #3 and at 2.45 K for sample #4.

Instead of measuring I-V curves at a bunch of fixed magnetic fields, it is more practical to measure the voltage (or resistance) with a fixed temperature (for example, in our ^{4}He flow-type refrigerator, at 2.47±0.01 K) as well as with a fixed measurement current I_m above I_c (see Fig. S5 and Table I), and to sweep the magnetic field, as demonstrated in Ref. S7. This method enables us (1) to avoid any temperature fluctuations around the superconducting transition temperature of Bi/Ni $T_\mathrm{c}^{\mathrm{Bi/Ni}} \approx 4$ K, where the temperature fluctuation is more than 100 mK for our ^{4}He flow-type refrigerator and (2) to measure LP oscillations of Bi/Ni and Nb ring-shaped devices simultaneously although they have different superconducting critical temperatures ($T_\mathrm{c}^{\mathrm{Bi/Ni}} \approx 4$ K and $T_\mathrm{c}^{\mathrm{Nb}} \approx 5$ K). We note that the phase of the oscillations in R vs H curves is opposite to that in I_c vs H as well as T_c vs H[S6, S7].

In Tables I and II, we list Bi/Ni and Nb ring-shaped devices used in the present work.

Table I| Properties of Bi/Ni ring-shaped devices.

Sample number	T_c [K]	I_c [μA] at ≈ 2.5 K at $\mu_0 H = 0$ mT	$\mu_0 H_0$ [mT]
1	4.0	50	0.96
2	4.0	51	0.95
3	3.9	20	0.62
4	4.0	20	0.65

Table II| Properties of Nb ring-shaped devices.

Sample number	T_c [K]	I_c [μA] at ≈ 2.5 K at $\mu_0 H = 0$ mT	$\mu_0 H_0$ [mT]
1	5.1	3.4×10^2	0.84
2[S8]	5.3	2.4×10^2	1.45

3. How to analyze the LP oscillations

In this section, we describe the evaluation methods of LP oscillations observed in Bi/Ni ring-shaped devices. We first determined the real zero magnetic field to evaluate the phase of the resistance oscillations. As mentioned in the main text, there should be a small offset magnetic field due to remnant magnetization of iron core of electromagnet and terrestrial magnetism. The offset of zero magnetic field was determined by measuring a Nb ring-shaped device simultaneously. We found that the resistance local minimum of the Bi/Ni ring-shaped device is placed at the same field as that of the Nb reference device [see Fig. 2b]. Based on this analysis, we fixed the real zero magnetic field.

Then, we normalize the horizontal axis by dividing it by the value corresponding to one magnetic flux quantum ϕ_0 calculated from the ring area. In Fig. S7, the schematic image of a ring-shaped device is illustrated. Because the ring has a finite width (in the present case, $\approx$ 500 nm), the area S for one magnetic flux quantum to pass through depends on the definition. For example, if the center part of the ring (indicated by the dotted line in Fig. S7) is taken as the side length, $S = (1.4 \times 1.4)$ μm^2 and the corresponding magnetic field $\mu_0 H_0$ is 1.06 mT by using $\mu_0 H_0 = \phi_0 / S$.

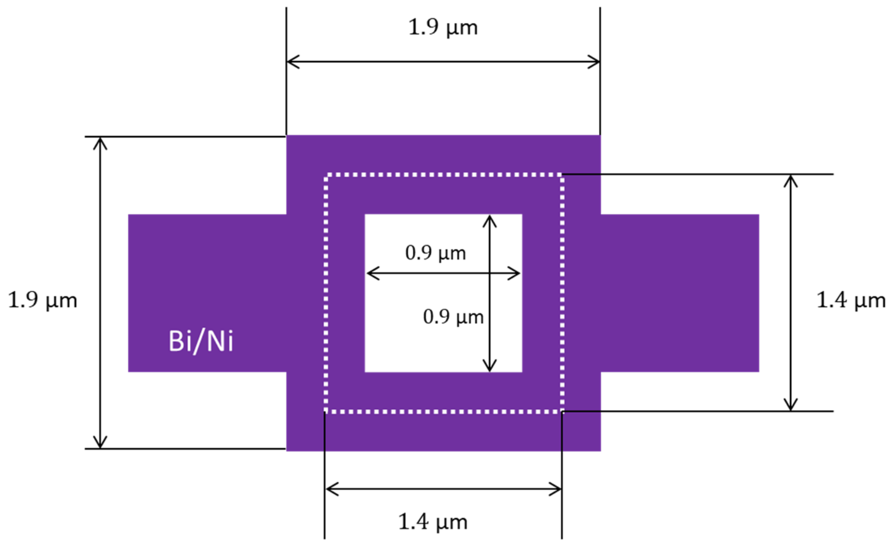

Fig. S7| Schematic image of a ring-shaped device (samples #1 and #2). From this structure, the maximum and minimum areas for one magnetic flux quantum to pass through are $S = (0.9 \times 0.9)$ μm^2 and (1.9×1.9) μm^2, respectively. The dotted line indicates the center of the ring width and the side length is 1.4 μm. Thus, $\mu_0 H_0$ ranges from 0.57 mT to 2.56 mT.

Figure S8 is the same data set as in Fig. 2 in the main text, but the horizontal axis is normalized by (**a**) $\mu_0 H_0 = 1.06$ mT and (**b**) $\mu_0 H_0 = 0.96$ mT. Resistance local minima and maxima should be located at the integer magnetic flux (H/H_0) for QFs-type and HQF-type LP oscillations, respectively. However, Fig. S8a does not satisfy such quantization conditions. In order to satisfy the quantization condition, the $\mu_0 H_0$ value was reduced, and we obtained $\mu_0 H_0 = 0.96$ mT as the suitable value because resistance local minima and maxima are placed at small integer numbers ($n \lesssim 6$) and at large integer numbers ($n \gtrsim 10$), respectively, as shown in Fig. S8b and Fig. 3 of the main text. The small difference in $\mu_0 H_0$ would originate from the device fabrication processes such as electron beam lithography and Ar milling. In fact, the estimated area is $S = (1.47 \times 1.47)\ \mu\mathrm{m}^2$ for $\mu_0 H_0 = 0.96$ mT. The estimated side length (1.47 μm) is only 5% longer than the ideal center part (1.4 μm) of the ring.

In order to confirm that the obtained value of $\mu_0 H_0 (= 0.96\ \mathrm{mT})$ is reasonable, we have adopted Fast Fourier Transformation (FFT) analysis. As shown in Fig. S9a, we first extracted the oscillation components by subtracting the background resistance (non-oscillating term) from Fig. 2a, and then performed FFT. The obtained FFT spectrum is shown in Fig. S9b as the blue solid line. Two sharp peaks are observed at around about $(\mu_0 H)^{-1} = 1.11\ (\mathrm{mT})^{-1}$ (indicated by the red arrow) and $1.02\ (\mathrm{mT})^{-1}$ (indicated by the green arrow), which correspond to $\mu_0 H = 0.90$ mT and $\mu_0 H = 0.98$ mT, respectively. This FFT analysis is seemingly inconsistent with Fig. S8b where the horizontal axis is normalized by $\mu_0 H_0 = 0.96$ mT. To solve this inconsistency, we fitted blue open circles in Fig. S9a with a function $f(x)$ which consists of two cosine functions:

$$f(x) = A(x)\cos\left(\frac{2\pi x}{\mu_0 H_0}\right) + B(x)\cos\left(\frac{2\pi x}{\mu_0 H_0} - \pi\right), \tag{3}$$

where $A(x) = -a\exp(-bx^2)$ and $B(x) = c\,[1 - \exp(dx)^2]\,/\{1 + \exp[g(x^2 - h^2)]\}$ express the magnetic field dependent amplitudes that include fitting parameters a, b, c, d, g, h, and $x = \mu_0 H$. We then performed FFT for this function. The FFT spectrum of the fitting function with $\mu_0 H_0 = 0.96$ mT is shown as the black solid line in Fig. S9b. This mimic function perfectly reproduces not only the two peak positions but also the ratio of the peak height between the two peaks. From these analyses, we can conclude that $\mu_0 H_0 = 0.96$ mT is the best value to normalize the horizontal axis in Fig. S8b.

In this way, a crossover from QFs- to HQFs-type LP oscillations was evaluated. By applying the same method, the crossover has been observed in other devices. The reproducibility of the crossover will be detailed in the next section.

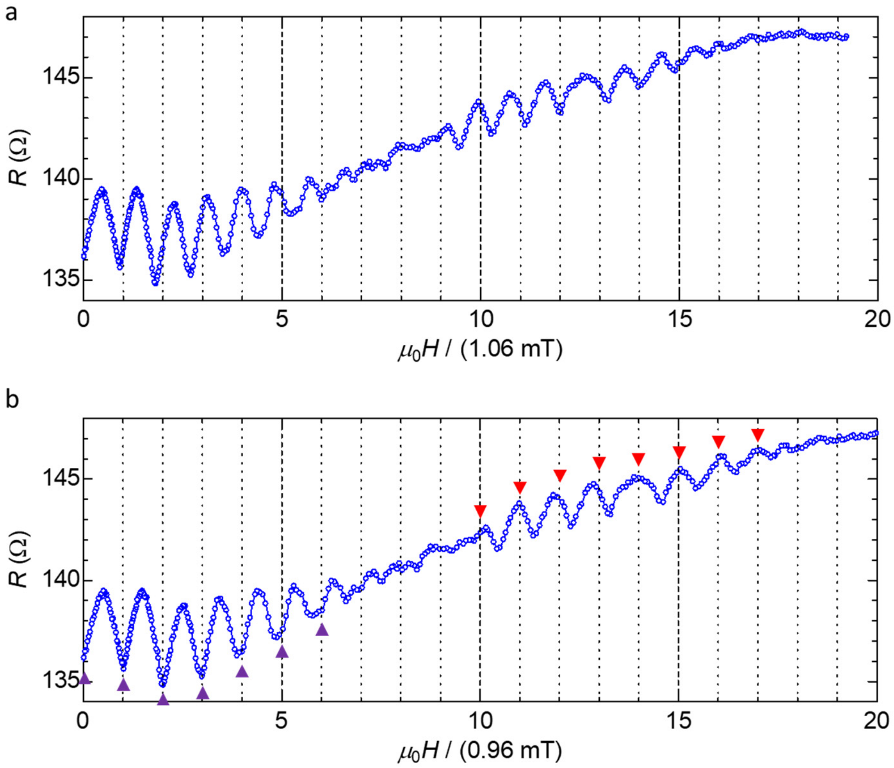

Fig| S8, LP oscillations as function of the magnetic field $\mu_0 H$ normalized by (**a**) $\mu_0 H_0 = 1.06$ mT and (**b**) $\mu_0 H_0 = 0.96$ mT. The purple triangles (red inverse triangles) indicate the positions of the local minima (maxima) at the integer numbers of magnetic flux.

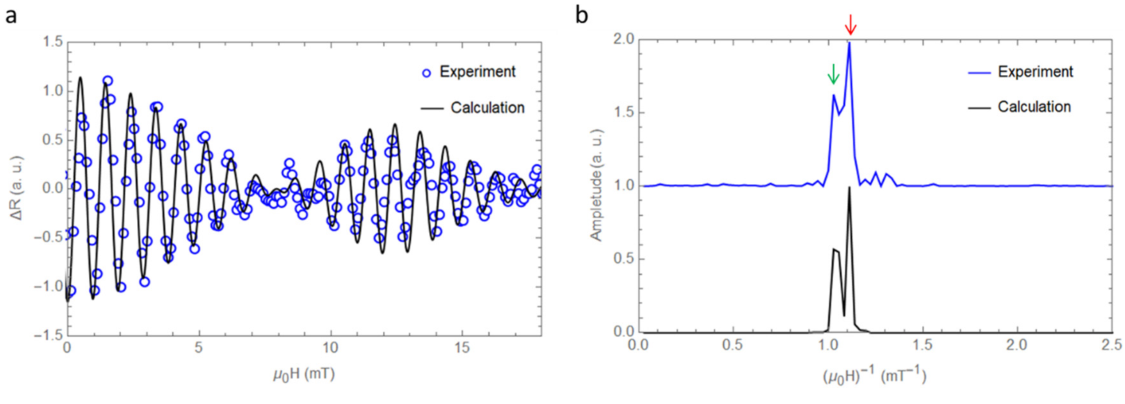

Fig. S9: (**a**) The oscillation component extracted from the raw data shown in Fig. 2a in the main text (blue open circle). The black solid line is the best fitting with Eq (3). (**b**) FFT analyses of the resistance oscillations and the fitting function shown in (a). The red and green arrows indicate the two peak positions.

4. Reproducibility of the crossover in LP oscillations

In order to confirm that the crossover from QFs- to HQFs-type LP oscillations is reproducible, we have performed some different experiments. We first investigated the LP oscillations with different I_m values using sample #1. As shown in Figs. S10 and S11, the crossover is very reproducible for various I_m and the crossover magnetic field H^* is almost constant at around 8 mT.

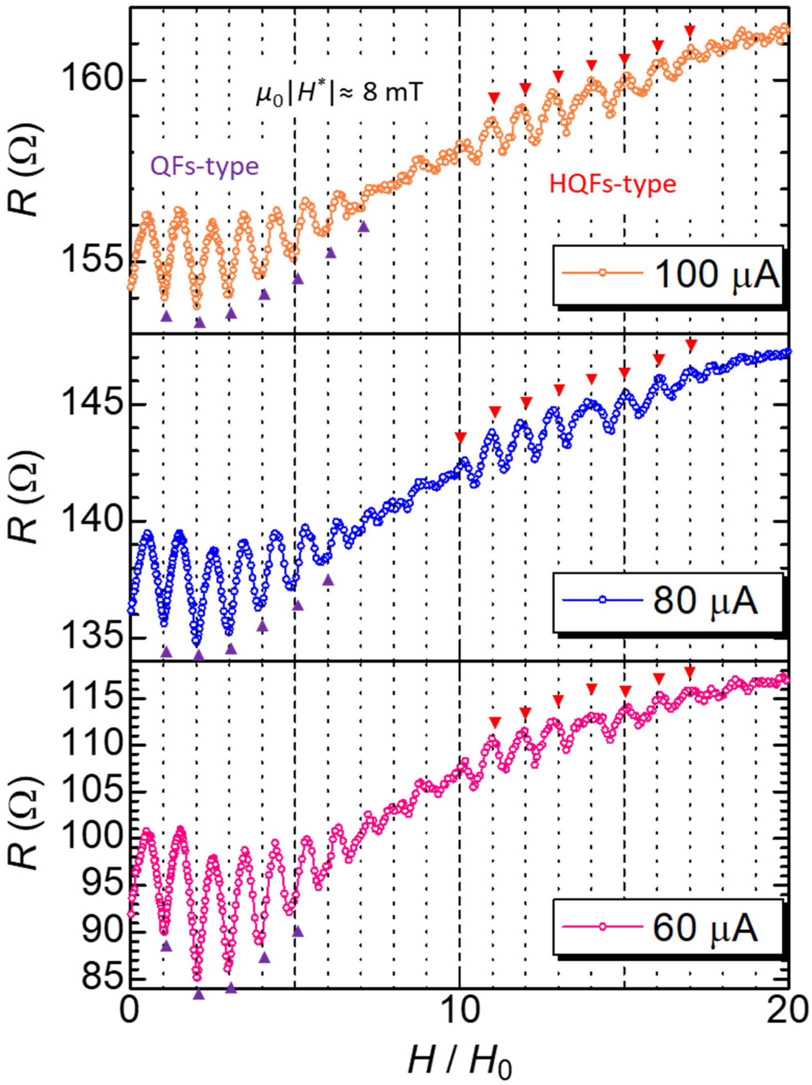

Fig. S10| LP oscillations measured with sample #1 using various I_m at 2.47 K in the positive magnetic field region. The purple triangles (red inverse triangles) indicate the positions of the local minima (maxima) at the integer numbers of magnetic flux.

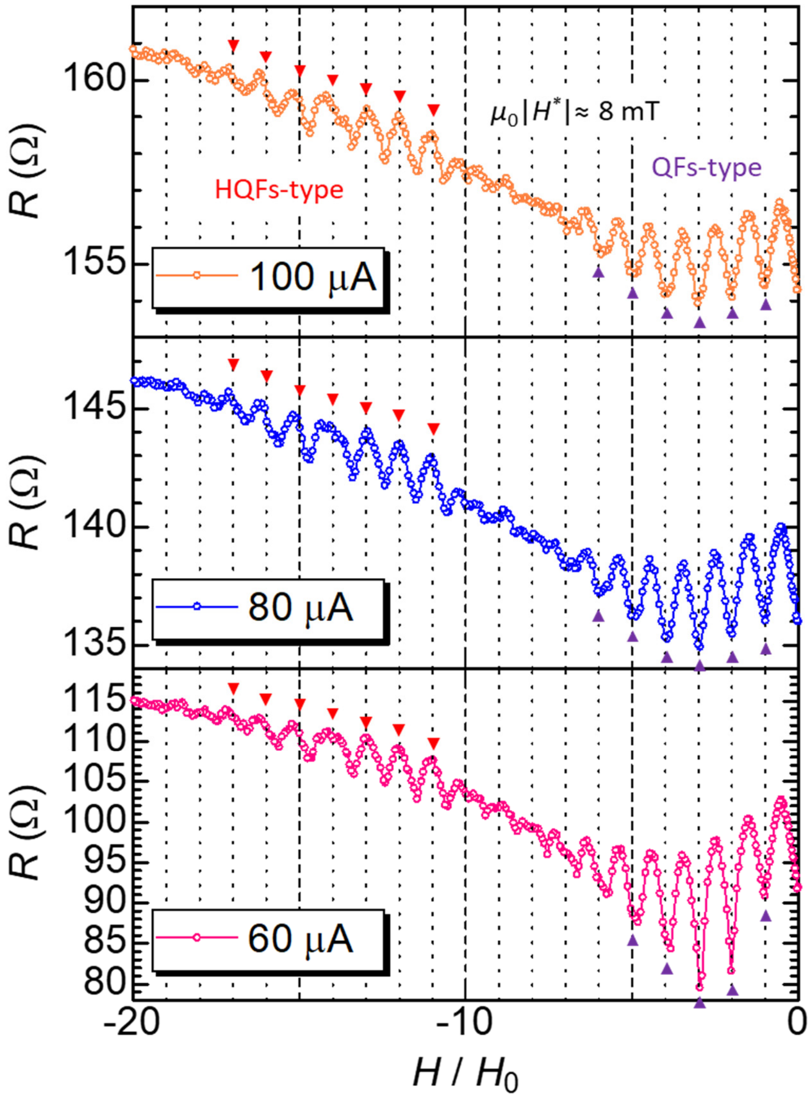

Fig. S11| LP oscillations measured with sample #1 using various I_m at 2.47 K in the negative magnetic field region. The purple triangles (red inverse triangles) indicate the positions of the local minima (maxima) at the integer numbers of magnetic flux.

Next, we show the reproducibility of the crossover from QFs- to HQFs-type LP oscillations using different devices. Some basic properties of ring-shaped devices fabricated with Bi/Ni are summarized in Tables 1. In Figs. S12 and S13, we show the LP oscillations obtained from sample #2 with various I_m and sample #3, respectively. Although large background resistances were superimposed on the LP oscillations as shown in Figs. S12(a) and S13, the switching between QFs-type and HQFs-type takes place at around $|H^*| \approx 8$ mT for both devices (see Figs. S12(b), S12(c), and the inset of Fig. S13). Because the background resistance was sometimes observed with a simple wire device as shown in Fig. S14, the origin of the background resistance is presumably due to the magnetoresistance which is peculiar to a mesoscopic device fabricated from the Bi/Ni bilayer film.

To summarize this section, the crossover from QFs- and HQFs-type LP oscillations is reproducible with different I_{m} values and in other devices with different ring sizes.

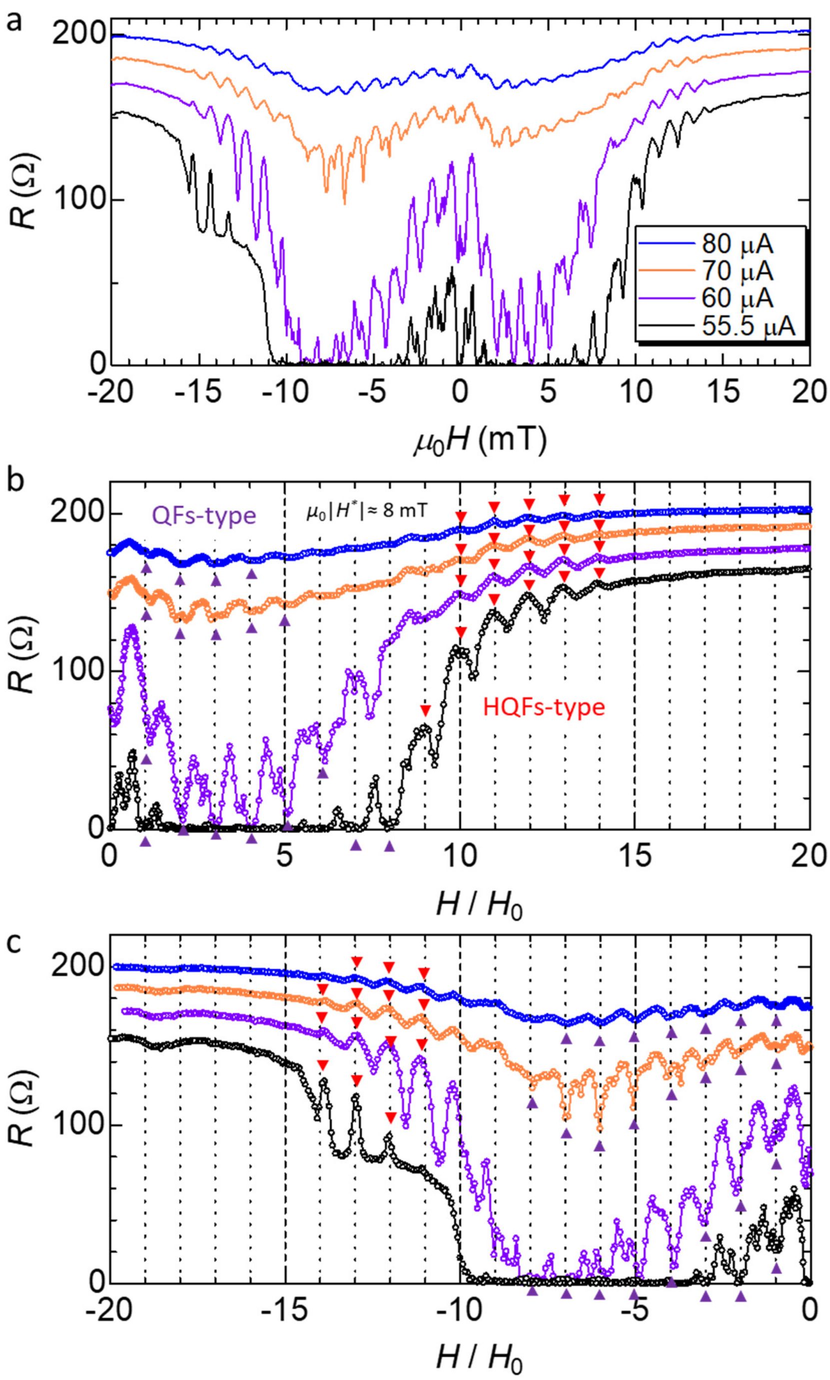

Fig. S12| (**a**) I_m dependence of LP oscillations measured with sample #2 at 2.46 K. The resistance oscillations after the normalization of the horizontal axis by $\mu_0 H_0$ in the positive and negative magnetic field regions are displayed in (**b**) and (**c**), respectively. The purple triangles (red inverse triangles) indicate the positions of the local minima (maxima) at the integer numbers of magnetic flux.

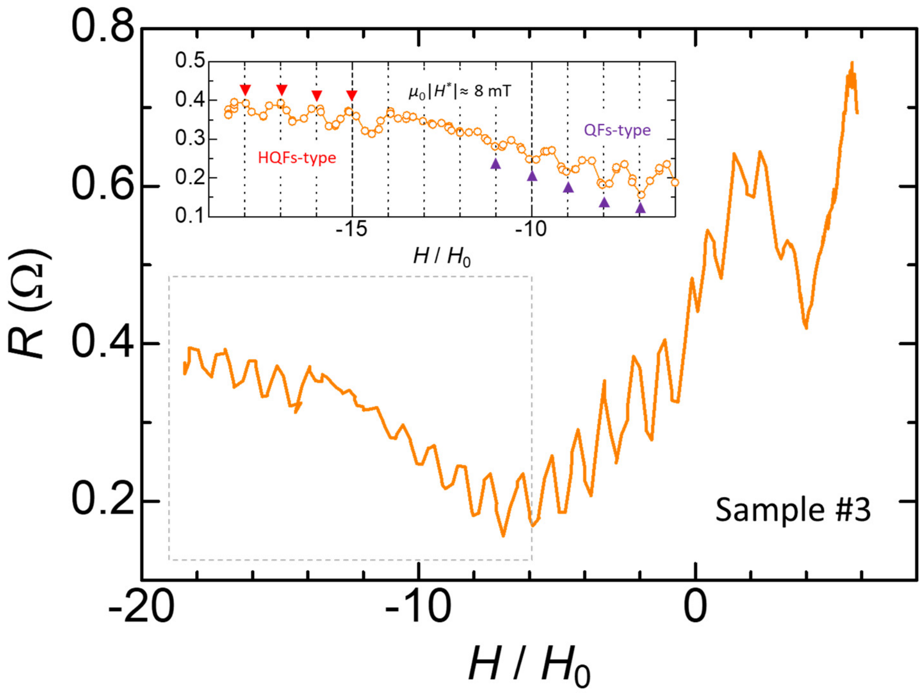

Fig. S13| LP oscillations measured with sample #3 at 2.34 K with $I_{\mathrm{m}} = 10$ μA. The inset shows a closeup view of the crossover region surrounded by the gray dotted square in the main panel. The purple triangles (red inverse triangles) indicate the positions of the local minima (maxima) at the integer numbers of magnetic flux.

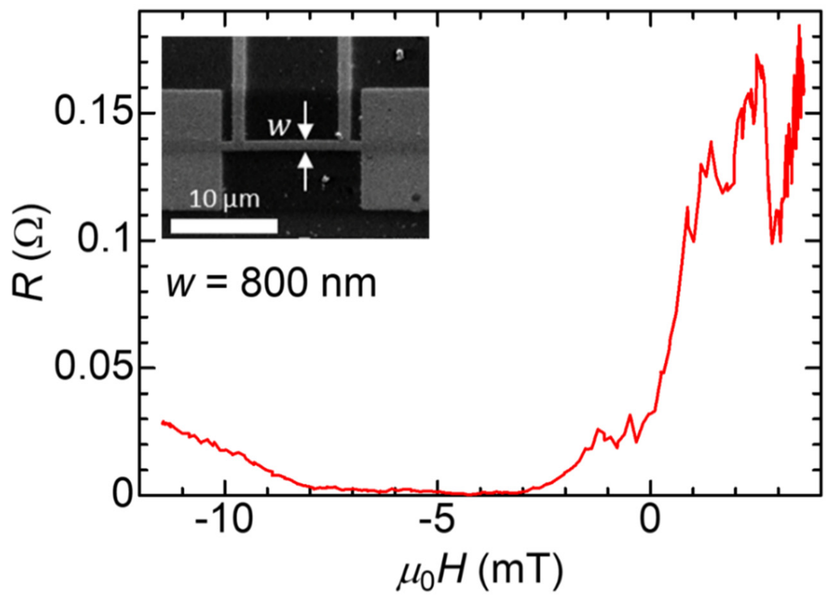

Fig. S14| Magnetoresistance measured with a Bi/Ni wire device at 2.34 K. The inset shows a scanning electron microscope image of the wire device.

5. Additional discussions on the crossover in LP oscillations

In the main text, we explain the crossover from QFs-type to HQFs-type LP oscillations based on a spin triplet superconductor with spin-orbit interaction, and also mention some possibilities which can be ruled out by the additional experiments. In this section, we add more detailed discussions for the mechanism of the crossover.

Here we raise all the possible scenarios which could explain the phase shift of LP oscillations: (1) the stray field of perpendicularly polarized Ni through the ring, (2) pining (or penetration) of magnetic vortices, induced by the external magnetic field or the measurement current I_{m}, inside the Bi/Ni ring, (3) superconducting weak links formed in the Bi/Ni ring, (4) the two-dimensional superconductivity on the top surface of Bi/Ni, and (5) the spin texture in spin-triplet superconducting rings with a spin-orbit interaction under a bias current.

We add some discussions on the scenario (2) where magnetic vortices induce the phase shift of the LP oscillations. According to Ref. S9, the lower critical field along the in-plane direction $\mu_0 H_{\mathrm{c1}}^{\parallel}$ is about 10 mT. In the present case, the magnetic field is applied along the out-of-plane direction. As will be detailed in the next section, there is a strong anisotropy for the upper critical filed H_{c2}: the in-plane upper critical field $\mu_0 H_{\mathrm{c2}}^{\parallel}$ is 5.5 times larger than the out-of-plane upper critical field $\mu_0 H_{\mathrm{c2}}^{\perp}$ at 2.5 K. By assuming the same anisotropy factor as the upper critical field, the lower critical field along the out-of-plane direction $\mu_0 H_{\mathrm{c1}}^{\perp}$ would be about a few mT. In other words, magnetic vortices should already be induced at a few mT. In this situation, the measurement current I_{m} should affect the vortex pinning and depinning, i.e., the voltage derived from vortex motion. However, the crossover does not depend on I_{m}. In addition, the crossover is reproducible for different devices with different ring sizes. These experimental facts can rule out the possibility that magnetic vortices pinned at defects, randomly distributed in the rings, move inside the ring and thus add a HQF to the ring.

As for the scenario (3), although our ring-shaped devices have no Josephson junctions artificially, superconducting weak links could be formed due to crystalline boundaries[S7] or phase slip lines induced by injecting a large current[S10]. The former case has already been denied by the cross-sectional scanning transmission electric microscopy (TEM) image which shows that the Bi/Ni bilayer is well-crystalized at each layer and has no domain boundaries[S1]. On the other hand, the latter case is required to check carefully. If a superconducting loop has weak links in the loop, switching between QFs-type and HQFs-type LP oscillations can be observed even in conventional superconductors, depending on the injected current and magnetic field[S11-S14]. According to Ref. S11, when the injected current is small enough, the switching from QFs-type to HQF-type LP oscillations occurs at higher magnetic fields, while the crossover magnetic field H^* is shifted to the lower magnetic field side as the injected current increases and eventually HQFs-type LP oscillations take place even at zero magnetic field. As shown in Figs. S10 and S11, however, H^*

is almost constant at around 8 mT for various I_{m} values in the Bi/Ni ring-shaped device (sample #1). This result obviously demonstrates that there is no accidental formation of superconducting weak links, phase slip lines, or magnetic vortices in the ring-shaped device.

In the scenario (4), the two-dimensional (more precisely, surface) state at the Bi layer plays an important role in the unconventional superconductivity. Here we add further information to exclude the possibility of the scenario (4). According to Refs. S15, S16, and S17, a surface state such as the Rashba effect is essential. In two-dimensional surface superconductors with the strong Rashba effect such as the Bi_2Se_3/monolayer $NbSe_2$ system [S18], it is known that the $\mu_0 H_{\mathrm{c2}}$ for an in-plane magnetic field often exceeds the Pauli limiting field $\mu_0 H_{\mathrm{P}} = 1.86 T_{\mathrm{c}}$, showing a $\sqrt{T_{\mathrm{c}} - T}$ dependence. If there is a dominant surface contribution from a strong Rashba coupling in the present system with $T_{\mathrm{c}}^{\mathrm{Bi/Ni}} \approx 4$ K and thus $\mu_0 H_{\mathrm{P}} = 7.44$ T, such a characteristic behavior should be observed in $\mu_0 H_{\mathrm{c2}}$. As mentioned in the main text and also will be detailed in Sec. 6, however, the measured in-plane $\mu_0 H_{\mathrm{c2}}$ neither exceeds the Pauli-limiting field $\mu_0 H_{\mathrm{P}} = 7.44$ T nor exhibits the $\sqrt{T_{\mathrm{c}} - T}$ dependence, but can rather be explained by the standard three-dimensional Ginzburg-Landau theory with a strong anisotropy. Thus, from the experimental point of view, the Rashba effect is negligibly small in the present Bi/Ni bilayer. In addition, for the out-of-plane magnetic field of our interest, the $\mu_0 H_{\mathrm{c2}}$ is far below $\mu_0 H_{\mathrm{P}}$, suggesting that the orbital pair-breaking effect is dominant.

From the theoretical viewpoint, the effective p-wave-like superconducting state is possible by considering the Rashba Hamiltonian at the top of Bi layer, an s-wave superconductivity induced by a possible formation of Bi_3Ni layer at the interface between Bi and Ni, and a Zeeman field[S17]. However, even in such a case, the crossover from QFs- to HQFs-type LP oscillations cannot be expected, based on the following theoretical reasons. In p-wave superconducting states, the **d**-vector, which is the order parameter of the spin-triplet superconductors (see Sec. 7 for the definition), is indispensable for the realization of HQFs. The HQFs is accompanied by the π-jump of the U(1) phase of the order parameter, which can be compensated by flipping the **d**-vector as $d \rightarrow -d$. In spin-orbit coupled systems, however, the **d**-vector is fully polarized by the spin-orbit coupling. As discussed in Sec. 7, the effective p-wave pairing scenario induced by proximitized s-wave superconductivity cannot support the HQFs-like LP oscillations. In Sec. 7, we will also clarify that the interplay of spin-orbit interaction with the magnetic texture of the Ni layer may cause the shift the LP oscillation but cannot explain the HQFs-like LP oscillations.

As will be discussed in Sec. 8, in the scenario (5), the HQFs accompanied by the spin texture are preferable to QFs when both the perpendicular field and the in-plane field $\mathbf{H}_{\mathrm{M}}$ are present. The transverse field $\mathbf{H}_{\mathrm{M}}$ stems from a stray field from the Ni layer. As demonstrated in Ref. S9, in the Bi/Ni bilayer film, a clear Meissner signal was observed even at 0 mT. The magnitude of the signal is suppressed when the in-plane magnetic field of ~1 mT is applied. In addition, the sign of the Meissner signal at 0 mT changes when the magnetization direction of the Ni layer is switched. These facts indicate that there exists a stray field from the Ni layer even below T_c and the magnitude of the in-plane stray field can be estimated to be ~1 mT. This in-plane stray field from the Ni layer should work as $\mathbf{H}_M$ in the Bi/Ni bilayer.

6. Upper critical field measurements in Bi/Ni bilayer film

In order to evaluate the dimension of the superconductivity of our Bi/Ni film, the upper critical field $\mu_0 H_{c2}$ was measured. In this work, $\mu_0 H_{c2}$ is defined as the external magnetic field when the resistance becomes a half of the normal state resistance R_N. The samples were cooled down to about 40 mK by using a dilution refrigerator. The external magnetic field from 0 to 11 T was applied by a superconducting magnet.

The resistance of Bi/Ni film along the out-of-plane and in-plane magnetic fields at various temperatures T are shown in Fig. S15. The definitions of the magnetic field directions are the same as in Fig. S1. The vertical axis is normalized by R_N. As T decreases, $\mu_0 H_{c2}$ is shifted to the higher magnetic field side and the transition from the superconducting state to the normal state becomes broader in both cases. From the comparison between the two cases, the superconductivity of Bi/Ni bilayer is weaker for the out-of-plane magnetic field, which is common behavior for thin-film superconductors.

Figure S16 shows the temperature dependence of $\mu_0 H_{c2}$ for both the out-of-plane and in-plane magnetic field directions. In the vicinity of $T = 0$, the in-plane upper critical field $\mu_0 H_{c2}^{\parallel}$ is 4.4 times larger than the out-of-plane upper critical field $\mu_0 H_{c2}^{\perp}$. According to the Ginzburg-Landau theory for an anisotropic superconductor, the temperature dependence of $\mu_0 H_{c2}$ can be expressed as follows:

$$\mu_0 H_{c2}^{\perp}(T) = \frac{\phi_0}{2\pi\xi_{\parallel}^2}\left(1-\frac{T}{T_c}\right) \ , \tag{4}$$

$$\mu_0 H_{c2}^{\parallel}(T) = \frac{\phi_0\sqrt{12}}{2\pi\xi_{\parallel}d_{sc}}\left(1-\frac{T}{T_c}\right)^{\alpha}, \tag{5}$$

where $\xi_{\parallel}$ is the in-plane coherence length, and d_{sc} is the thickness of superconductor which is an important length scale rather than the out-of-plane coherence length $\xi_{\perp}$ as long as the system is two-dimensional, i.e., $\xi_{\perp} > d_{sc}$[S19-S25]. The power α is a fitting parameter. When the superconductivity is two-dimensional, $\alpha = 1/2$. On the other hand, α is close to 1 for a three-dimensional (i.e., bulk) superconductor. In such a case, d_{sc} becomes less important than $\xi_{\perp}$, and the coefficient of Eq. (5) is replaced by $\phi_0/(2\pi\xi_{\parallel}\xi_{\perp})$. Although $\mu_0 H_{c2}^{\perp}$ can be fitted well by Eq. (4) (see the orange solid line in Fig. S16), $\mu_0 H_{c2}^{\parallel}$ cannot be explained by Eq. (5) with $\alpha = 1/2$ (see the purple dotted line in Fig. S16); alternatively, $\alpha = 0.67$ in Eq. (5) can give a reasonable fitting (see the purple solid line in Fig. S16). From the relations $\mu_0 H_{c2}^{\perp} = \phi_0/(2\pi\xi_{\parallel}^2)$ and $\mu_0 H_{c2}^{\parallel} = \phi_0/(2\pi\xi_{\parallel}\xi_{\perp})$ at $T = 0$ [S23] and by using $\mu_0 H_{c2}^{\perp} = 1.44$ T and $\mu_0 H_{c2}^{\parallel} = 6.25$ T, we obtain $\xi_{\parallel} = 15.1$ nm and $\xi_{\perp} = 3.5$ nm. Because $\xi_{\perp}$ is 10 times smaller than the thickness of Bi/Ni film $d_{Bi/Ni}$ (= 37 nm), we conclude that our Bi/Ni film is an anisotropic three-dimensional superconductor, which is not consistent with the scenario in Ref. S17 where the two-dimensional superconductivity on the top surface of Bi/Ni plays an important role on the appearance of topological superconducting state. The importance of the superconductivity at the surface of the Bi layer and also at the boundary between Bi and Ni layers have been pointed out[S1,S26], but our results suggest that the bulk superconductivity is also important for understanding the superconductivity of Bi/Ni bilayer. This is consistent with the previous work which pointed out the importance of bulk superconductivity of Bi/Ni bilayer[S27].

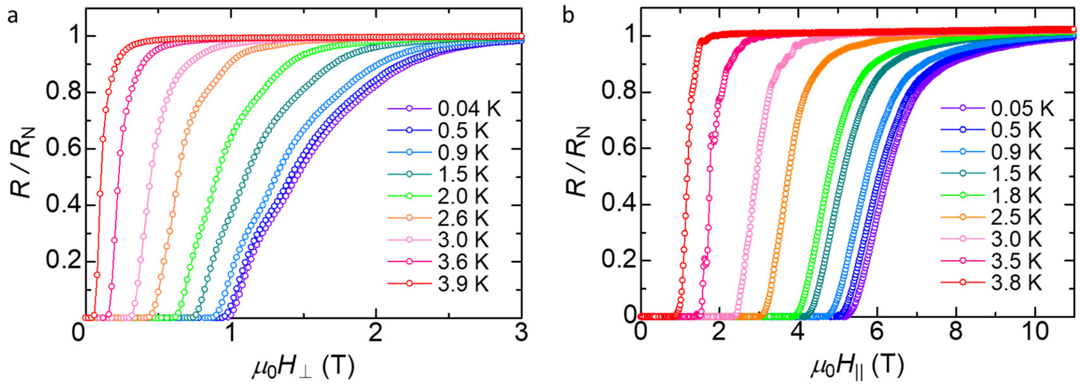

Fig. S15| Resistance of a Bi/Ni film normalized by R_{N} as a function of (**a**) the out-of-plane magnetic field and (**b**) the in-plane magnetic field, measured at various temperatures.

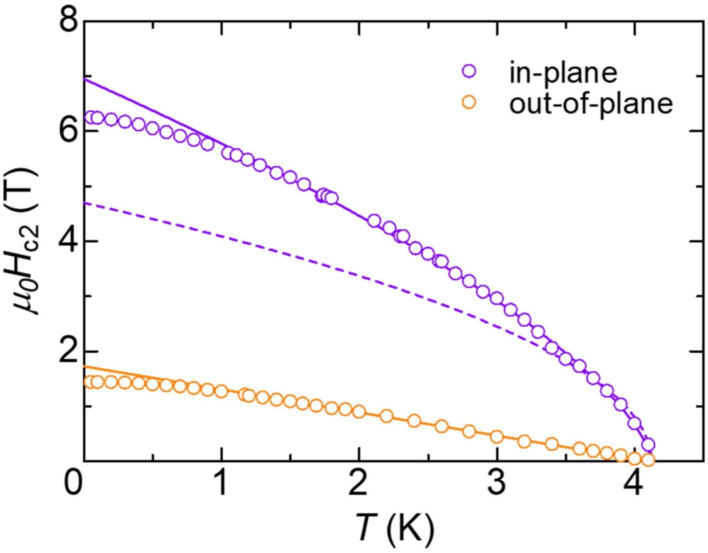

Fig. S16| Temperature dependence of the upper critical fields $\mu_0 H_{\mathrm{c2}}$ along the in-plane direction (purple open circle) and the out-of-plane direction (orange open circle). For the in-plane critical magnetic field, the experimental data are fitted by Eq. (4) with $\alpha = 1/2$ (purple dotted line) and with $\alpha = 0.67$ (purple solid line). For the out-of-plane critical magnetic field, the experimental data are fitted by Eq. (3) (orange solid line).

7. Effect of spin-orbit coupling on the LP oscillation

In this section, we focus on an effective p-wave pairing scenario based on the Rashba Hamiltonian at the top of the Bi layer[S17], and discuss the possibility of the crossover from QFs to HQFs in the LP oscillations. The key ingredients of the Hamiltonian are (i) spin-orbit interaction, (ii) s-wave superconductivity, (iii) an exchange or Zeeman field which arises from the electrons on the Bi surface, (iv) the superconducting Bi_3Ni alloy at the interface between Bi and Ni, and (v) the magnetic order of the Ni layer. We first demonstrate that the effective p-wave pairing state realized in such spin-orbit coupled systems cannot support the HQFs-like LP oscillations. Then, we examine how the interplay of spin-orbit interaction with the magnetic texture of the Ni layer affects the LP oscillation.

Let $\widehat{\Delta}(\boldsymbol{p},\boldsymbol{r})$ be the 2×2 spin matrix of the superconducting order, where $\boldsymbol{p}$ and $\boldsymbol{r}$ are the relative momentum and the center-of-mass coordinate of the Cooper pairs, respectively. The quantized flux state is expressed as

$$\widehat{\Delta}(\boldsymbol{p},\boldsymbol{r}) = e^{i\varphi(\theta)}\widehat{\Delta}(\boldsymbol{p},\rho), \tag{6}$$

where we assume the uniformity along the z-axis and $\boldsymbol{r}=(\rho,\theta,z)$ is the cylindrical coordinate. The $\mathrm{U}(1)$ phase $\varphi(\theta)$ is represented by the vorticity κ as $\varphi(\theta)=\kappa\theta$. In conventional s-wave superconductors, the vorticity is restricted to an integer value $\kappa\in\mathbb{Z}$ because of the single-valued order parameter. The HQF states are characterized by a half integer $\kappa=(2n+1)/2$ $(n\in\mathbb{Z})$, where the $\mathrm{U}(1)$ phase along the azimuthal direction changes from 0 to $(2n+1)\pi$ accompanied by the π-phase jump. However, such π-phase jump can be canceled out by the internal (spin or orbital) degrees of freedom of $\widehat{\Delta}$. To see this, we decompose $\widehat{\Delta}$ to the spin-singlet even-parity component $\psi(\boldsymbol{p})=\psi(-\boldsymbol{p})$ and the spin-triplet odd-parity component $\boldsymbol{d}(\boldsymbol{p})=-\boldsymbol{d}(-\boldsymbol{p})$ as

$$\widehat{\Delta}(\boldsymbol{p},\boldsymbol{r}) = \begin{pmatrix} \Delta_{\uparrow\uparrow}(\boldsymbol{p},\boldsymbol{r}) & \Delta_{\uparrow\downarrow}(\boldsymbol{p},\boldsymbol{r}) \\ \Delta_{\downarrow\uparrow}(\boldsymbol{p},\boldsymbol{r}) & \Delta_{\downarrow\downarrow}(\boldsymbol{p},\boldsymbol{r}) \end{pmatrix} = \psi(\boldsymbol{p},\boldsymbol{r})i\sigma_y + i\boldsymbol{d}(\boldsymbol{p},\boldsymbol{r})\cdot\boldsymbol{\sigma}\sigma_y, \tag{7}$$

where $\boldsymbol{\sigma}=(\sigma_x,\sigma_y,\sigma_z)$ are the Pauli matrices in the spin space. Let R_n be the n fold rotation operator for the z-axis. In the $d_{x^2-y^2}$ superconducting state, i.e., $\psi(\boldsymbol{p})=\Delta_0(p_x^2-p_y^2)$ and $\boldsymbol{d}=\boldsymbol{0}$, the operator rotates the order parameter as $R_4\psi(\boldsymbol{p})=-\psi(\boldsymbol{p})$, which compensates the discontinuity of the $\mathrm{U}(1)$ phase $\varphi(\theta=0)=-\varphi(\theta=\pi)$. Indeed the half magnetic flux with $\phi=\phi_0/2$ has been observed in a trigrain boundary-junction ring of superconducting $\mathrm{YBa_2C_3O_{7-\delta}}$[S28]. For spin-triplet superconductors with $\boldsymbol{d}(\boldsymbol{p})=\widehat{\boldsymbol{d}}f(\boldsymbol{p})$, the π-phase jump arising from the half-winding of the $\mathrm{U}(1)$ can also be canceled out by flipping $R_2\widehat{\boldsymbol{d}}=-\widehat{\boldsymbol{d}}$. The half-quantum vortices have been observed in superfluid ^{3}He with uniaxially anisotropic disorders, which is a prototype of spin-triplet superfluids[S29]. Hence, the HQF state can be realized by the texture of the spin or orbital component of the order parameter.

Consider the electrons on the Bi surface with proximitized s-wave pairing. Here we demonstrate that although spin-orbit coupling induces an effective p-wave pairing, the spins of the Cooper pairs are frozen out and not responsible for the HQF-type LP oscillation. Following Ref. S17, we consider that two-dimensional electrons on the Bi surface and an s-wave superconductivity, $\hat{\Delta} = \Delta i\sigma_y$, proximitized from the superconducting alloy Bi_3Ni formed at the interface between Bi and Ni, where we set $\Delta \in \mathbb{R}$ without loss of generality. The Bogoliubov-de Gennes Hamiltonian is given by

$$\mathcal{H}(\boldsymbol{p}) = \begin{pmatrix} \hat{\varepsilon}(\boldsymbol{p}) & \Delta i\sigma_y \\ -\Delta i\sigma_y & -\hat{\varepsilon}^{\mathrm{tr}}(-\boldsymbol{p}) \end{pmatrix}. \tag{8}$$

The 2×2 matrix, $\hat{\varepsilon}(\boldsymbol{p}) = \varepsilon_0(\boldsymbol{p}) + \boldsymbol{g}(\boldsymbol{p}) \cdot \boldsymbol{\sigma} + \boldsymbol{B} \cdot \boldsymbol{\sigma}$, is the Hamiltonian for the normal electrons on the Bi surface, where $\boldsymbol{g}(\boldsymbol{p}) = -\boldsymbol{g}(-\boldsymbol{p})$ is antisymmetric spin-orbit coupling and $\boldsymbol{B}$ is the exchange field arising from the magnetic moment of the Ni layer and an applied magnetic field. To clarify how the spin-triplet odd-parity pairing emerges from the conventional s-wave gap, we introduce the unitary matrix[S30], $U = (\tau_0 + i\sigma_y\tau_x)/\sqrt{2}$, where τ_0 and τ_x are the unit matrix and the Pauli matrix in the particle-hole space, respectively. The unitary transformation of the BdG Hamiltonian reads

$$U\mathcal{H}(\boldsymbol{p})U^{\dagger} = \begin{pmatrix} \boldsymbol{B} \cdot \boldsymbol{\sigma} + \Delta & -\varepsilon_0(\boldsymbol{p})i\sigma_y - i[\boldsymbol{\sigma} \cdot \boldsymbol{g}(\boldsymbol{p})]\sigma_y \\ \varepsilon_0(\boldsymbol{p})i\sigma_y + i[\boldsymbol{\sigma} \cdot \boldsymbol{g}(\boldsymbol{p})]\sigma_y & -\boldsymbol{B} \cdot \boldsymbol{\sigma}^{\mathrm{tr}} - \Delta \end{pmatrix}. \tag{9}$$

This shows that the transformed Hamiltonian is regarded as the admixture of the spin-singlet even-parity component and spin-triplet odd-parity component. As the effective $\boldsymbol{d}$-vector arises from the antisymmetric spin-orbit coupling $\boldsymbol{g}(\boldsymbol{p})$, the spin degrees of freedom of the Cooper pairs are frozen out. Therefore, the HQFs cannot be realized by the texture of the $\boldsymbol{d}$-vector in such spin-orbit systems with proximitized Δ.

In the rest of this section, let us discuss how the interplay of spin-orbit coupling with the magnetic texture of the Ni layer affects the LP oscillation. In the context of the Ginzburg-Landau (GL) theory, it has been known that in superconductors with broken inversion symmetry, a coupling between the magnetic field and the supercurrent can be induced by the so-called Lifshitz invariants

$$f_{\mathrm{LI}} = \sum_{ij} \kappa_{ij} B_i \left[\Delta^*(\boldsymbol{r})\left(\Pi_j \Delta(\boldsymbol{r})\right) + \Delta(\boldsymbol{r})\left(\Pi_j \Delta(\boldsymbol{r})\right)^*\right], \tag{10}$$

where $\boldsymbol{\Pi} = -i\boldsymbol{\nabla} + 2|e|\boldsymbol{A}$ is the gauge covariant derivative. Here we set $\hbar = c = 1$. Thus, the GL free energy functional for spin-orbit coupled superconductors under a magnetic field $\boldsymbol{B}$ is given by

$$f_{\mathrm{GL}} = K|\boldsymbol{\Pi}\Delta(\boldsymbol{r})|^2 + \alpha|\Delta(\boldsymbol{r})|^2 + \frac{\beta}{2}|\Delta(\boldsymbol{r})|^4 + \frac{\boldsymbol{B}^2}{8\pi} + f_{\mathrm{LI}}, \tag{11}$$

with the GL parameters $\alpha < 0$, $K > 0$, and $\beta > 0$. The Lifshitz invariant term describes a coupling between the magnetic texture of the Ni layer and the supercurrent density. The explicit expression of κ_{ij} depends on crystalline symmetry and broken inversion symmetry[S31,S32]. For the Rashba spin-orbit interaction, the tensor is given by $\kappa_{ij} = \sum_k \epsilon_{ijk}\hat{n}_k$, where $\hat{\boldsymbol{n}}$ is the unit vector associated with the broken inversion symmetry at the surface. Here we take the z-axis along the surface normal direction, i.e., $\hat{\boldsymbol{n}} = \hat{z}$. Then, only the transverse components of the magnetic field, $\boldsymbol{B} \perp \hat{z}$ contribute to the Lifshitz invariant term.

The Lifshitz invariant term provides a source of exotic superconducting phenomena[S31-S33]. This includes the spatially modulated pairing state known as the Fulde-Ferrell-Larkin-Ovchinnikov (FFLO) state and the magnetoelectric effect. The in-plane magnetic field together with a Rashba spin-orbit interaction shifts the center of the Fermi surfaces, leading to the formation of the Cooper pairs with nonzero center-of-mass momentum $\boldsymbol{Q}$. The FFLO state may be accompanied by the half-quantum flux as a half dislocation with π-phase winding[S34-S36]. As $\boldsymbol{Q} \parallel \boldsymbol{B} \times \hat{z}$, however, the realization of the FFLO state with a modulation along the ring, i.e., $\boldsymbol{Q} \parallel \hat{\boldsymbol{\theta}}$, requires both a special configuration of the in-plane field such as $\boldsymbol{B} \cdot \hat{\boldsymbol{\rho}} \neq 0$. In addition, the FFLO state is usually stabilized at lower temperatures $T \lesssim 0.5T_{\mathrm{c}}$ and strong in-plane magnetic fields[S36], which are not relevant to the current situation of the Bi/Ni bilayer that an external magnetic field is applied along $\hat{z}$ and the temperature is $T \approx 0.6T_{\mathrm{c}}$. Hence, it is difficult to expect the FFLO state with HQFs in the current situation.

Another important consequence of the Lifshitz invariants is the formation of the spontaneous current. As a combination with the magnetic texture of the Ni layer, the spontaneous current may flow along the ring as $\boldsymbol{j}_{\mathrm{soc}} \propto \kappa\hat{z} \times \hat{\boldsymbol{B}}$, which generates the additional contribution to the magnetic flux penetrating the superconducting ring and shifts the LP oscillations. The shift of the LP oscillations is not quantized but depends on the strength of the spin-orbit coupling and magnetic texture. To clarify this, we recast the GL free energy in Eq. (11) and obtain the following equation:

$$f_{\mathrm{GL}} = K\sum_j \left|\left(\Pi_j - \frac{\kappa(\boldsymbol{B}\times\hat{z})_j}{K}\right)\Delta(\boldsymbol{r})\right|^2 + \left(\alpha - \frac{\kappa^2(\boldsymbol{B}\times\hat{z})^2}{K}\right)|\Delta(\boldsymbol{r})|^2 + \frac{\beta}{2}|\Delta(\boldsymbol{r})|^4. \tag{12}$$

Here we assume that the in-plane magnetic field arising from the Ni layer slowly varies along the superconducting ring. Equation (12) indicates that the Cooper pairs experience the additional vector potential stemming from the Lifshitz invariant term as $A_j \to A_j - \kappa(B\times\hat{z})_j/2|e|K$, giving rise to the shift of the magnetic flux

$$\delta\phi \equiv \frac{\kappa}{2|e|K}\int(\boldsymbol{B}\times\hat{z})\cdot d\hat{\boldsymbol{l}} \approx -\frac{\kappa R}{2|e|K}\int_0^{2\pi} B_\rho(\theta)d\theta, \tag{13}$$

where $\hat{\boldsymbol{l}}$ is the unit vector along the azimuthal direction of the ring and $B_\rho = B_x\cos\theta + B_y\sin\theta$ is the radial component of the in-plane magnetic field. To estimate the magnitude of the shift, we utilize the GL parameters in the weak coupling limit, $K = 7\zeta(3)N(0)v_F^2/[32(\pi k_B T_c)^2]$ and $\kappa = 7\zeta(3)\delta N_0 g\mu_B v_F^2/[32(\pi k_B T_c)^2]$[S37], where g and μ_B are the g-factor and the Bohr magneton, respectively. We also introduced $N_0 \equiv (N_+ + N_-)/2$ and $\delta N_0 \equiv N_+ - N_-$ with the density of states of two bands split by the spin-orbit coupling, $N_\pm$. Equation (13) is then recast as follows:

$$\delta\phi = \frac{g(\delta N_0/N_0)}{2(k_F R)}\pi R^2 \int_0^{2\pi} B_\rho(\theta)d\theta. \tag{14}$$

We note that $\delta N_0/N_0$ measures the spin-orbit coupling and the particle-hole asymmetry in the normal electron state, which is of the order of $\kappa_0(T_c/T_F)$ (κ_0 is the strength of the spin-orbit coupling). The radius of the superconducting ring in the current situation is much larger than the Fermi wavelength k_F^{-1}, i.e., $k_F R \gg 1$. As mentioned in Sec. 5, the magnitude of the in-plan field is about 1 mT. Based on these parameters, we conclude that the spin-orbit interaction causes the negligibly small shift of the LP oscillations. In addition, the shift $\delta\phi$ depends on the magnetic texture and nonzero $\delta\phi$ requires a nontrivial spatial profile of $B_\rho(\theta)$. In Fig. S17, we display the three examples of the magnetic textures of the Ni layer. As $B_\rho = 0$ in the type-A and $B_\rho \propto \cos\theta$ in the type-B, both textures result in $\delta\phi = 0$. The texture of the type-C is responsible for the nonzero shift $\delta\phi$.

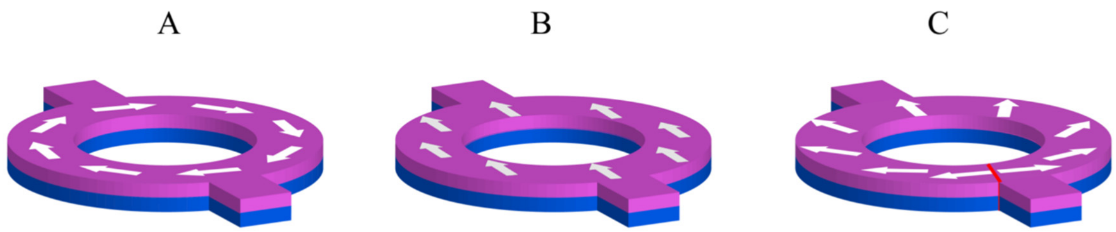

Fig. S17. Examples of the Ni magnetic textures, where the arrows depict the magnetic moment. The type-A and type-B shows $\delta\phi = 0$, while the texture of the type-C is responsible for the nonzero shift $\delta\phi$.

8. Theoretical interpretation of the phase shift in LP oscillations

In a Little-Parks (LP) experiment with a bias electric current, the resistivity should be associated with the critical bias current density j_c. It has theoretically been shown[S6] that j_c exhibits a LP oscillation similarly to the transition temperature and that at least within the conventional BCS theory, the oscillation pattern is not half-quantum-shifted even in the spin-triplet p-wave case where the $\mathbf{d}$-vector degrees of freedom may possibly lead to an exotic superconducting state such as a half-quantum vortex in the context of superfluid ^{3}He [S38]. Here, we demonstrate that a half-quantum-shifted LP oscillation in j_c can be realized in the presence of a spin-orbit coupling which is not taken into account in Ref. S6. In spin-triplet superconductors, the gap function is obtained by the 2×2 spin matrix, which is parameterized with the $\mathbf{d}$-vector having the momentum dependence $\mathbf{d} = (d_x(\mathbf{p}), d_y(\mathbf{p}), d_z(\mathbf{p}))$, as shown in Sec. 7. Since the detailed electronic structure relevant to superconductivity in the Bi/Ni system is not yet available, here we consider the isotropic Fermi surface for simplicity and assume that the p-wave pairing interaction is dominant as in the case of superfluid ^{3}He. The $\mathbf{d}$-vector is expressed as $d_\mu(\mathbf{p}) = \sum_i A_{\mu,i}\hat{p}_i$ with the order parameter $A_{\mu,i}$, and thus the GL free energy functional in the presence of a magnetic field is given by $\mathcal{F}_{\mathrm{GL}} = N(0)\int d\mathbf{r}\left[f^{(2)} + \delta f^{(2)} + \delta f_D^{(2)} + f^{(4)}\right]$ with

$$
\begin{aligned}
f^{(2)} &= \sum_{\mu,i,j}\left[\frac{\alpha}{3}A_{\mu,i}^* A_{\mu,i} + K' A_{\mu,i}^*\left(\Pi_j\Pi_j A_{\mu,i} + 2\Pi_i\Pi_j A_{\mu,j}\right)\right],\\
\delta f^{(2)} &= -\frac{\delta\alpha}{3} i \sum_i \left(A_{x,i}A_{y,i}^* - A_{y,i}A_{x,i}^*\right),\\
\delta f_{\mathrm{D}}^{(2)} &= \lambda_{\mathrm{D}} \sum_{\mu,\nu}\left(A_{\mu,\mu}^* A_{\nu,\nu} + A_{\mu,\nu}^* A_{\nu,\mu} - \frac{2}{3}A_{\mu,\nu}^* A_{\mu,\nu}\right),\\
f^{(4)} &= \sum_{\mu,\nu,i,j}\Big[\beta_1\left|A_{\mu,i}A_{\mu,i}\right|^2 + \beta_2\left(A_{\mu,i}^* A_{\mu,i}\right)^2 + \beta_3 A_{\mu,i}^* A_{\nu,i}^* A_{\mu,j}A_{\nu,j} + \beta_4 A_{\mu,i}^* A_{\nu,i} A_{\nu,j}^* A_{\mu,j}\\
&\qquad + \beta_5 A_{\mu,i}^* A_{\nu,i} A_{\nu,j} A_{\mu,j}^*\Big].
\end{aligned}
\tag{15}
$$

This functional form is obtained from $\mathcal{F}_{\mathrm{GL}}$ for superfluid ^{3}He by replacing $-i\nabla$ by $\boldsymbol{\Pi} = -i\nabla + 2|e|\mathbf{A}$ with the vector potential $\mathbf{A} = \frac{1}{2}\mathbf{H} \times \mathbf{r}$. Here, to simplify the notation, we take $\hbar = 1$ and $k_{\mathrm{B}} = 1$. In the weak coupling limit, the coefficients are given by $\alpha = \ln\frac{T}{T_{\mathrm{c0}}}$, $K' = \frac{1}{5}\left(\frac{T_{\mathrm{c0}}}{T}\right)^2 \xi_0^2$, and $-2\beta_1 = \beta_2 = \beta_3 = \beta_4 = \beta_5 = \frac{7\zeta(3)}{120\pi^2 T^2}$ with the superconducting transition temperature at zero field T_{c0} and the coherence length $\xi_0 = \sqrt{\frac{7\zeta(3)}{48\pi^2}}\frac{v_F}{T_{\mathrm{c0}}}$ at $T = 0$[S38]. The $\delta f^{(2)}$ term originates from the difference in density of states between the up-spin and down-spin Fermi surfaces and thereby, is active only in a magnetic field[S38,S39]. Within a linear approximation, we can express $\delta\alpha$ as $\delta\alpha = \eta\frac{\Phi}{\Phi_0}$. $N(0)$ is the density of states averaged over the Zeeman-split two Fermi surfaces. The $\delta f_{\mathrm{D}}^{(2)}$ term represents the dipole interaction, a kind of spin-orbit interaction, which is known to be important for texture formations in superfluid ^{3}He. λ_{D} is a coupling constant related to the dipole-type spin-orbit interaction. This dipole interaction is not incorporated in Ref. S6, and the following discussion is essentially the same as that in Ref. S6 except the $\delta f_{\mathrm{D}}^{(2)}$ term. From the GL free energy functional Eq. (15), one can derive the superconducting current density $\mathbf{j} = -\frac{\delta\mathcal{F}_{\mathrm{GL}}}{\delta\mathbf{A}}$ as follows:

$$j_\alpha = -4|e|N(0)K'\sum_{\mu,i,j} A_{\mu,i}^*\left(\delta_{ij}\Pi_\alpha + \delta_{\alpha j}\Pi_i + \delta_{\alpha i}\Pi_j\right)A_{\mu,j}. \tag{16}$$

With the combined use of Eqs. (15) and (16), one can calculate the superconducting critical current density which can be obtained by measuring I-V properties.

In the Bi/Ni superconductor, a chiral pairing state is proposed as a possible pairing symmetry. Thus, we assume the chiral p-wave state:

$$A_{\mu,i} = d_\mu w_{\mathbf{p},i} \tag{17}$$

where $w_{\mathbf{p},i} = \frac{1}{\sqrt{2}}\left(\hat{p}_x + i\hat{p}_y\right)$, i.e., the ABM state in the context of superfluid ^{3}He. At this point, the orbital degrees of freedom $w_{\mathbf{p},i}$ and the spin degrees of freedom d_μ are completely decoupled, and such a situation is also the case for $f^{(2)}$, $\delta f^{(2)}$, and $f^{(4)}$ in the GL free energy functional. The dipole interaction $\delta f_{\mathrm{D}}^{(2)}$, on the other hand, couples these momentum-space and spin-space degrees of freedom: $\delta f_{\mathrm{D}}^{(2)}$ is calculated as $\delta f_{\mathrm{D}}^{(2)} = \lambda_{\mathrm{D}}\left[\frac{1}{3}|\mathbf{d}|^2 - (\mathbf{d}\cdot\hat{p}_z)^2\right]$. The $\mathbf{d}$-vector tends to orient along the $\hat{p}_z$ direction. In this respect, the dipole interaction works as a kind of spin-orbit interaction.

In the spin space, there exists another constraint on the direction of the $\mathbf{d}$-vector. In the presence of a magnetic field or a uniform magnetization, the $\uparrow\downarrow$ Cooper pair becomes unfavorable. Thus, the $\mathbf{d}$-vector tends to orient perpendicularly to the spin polarization direction, i.e., $d_z = 0$. We note that $d_z = 0$ does not mean $(\mathbf{d}\cdot\hat{p}_z) = 0$, because the spin and momentum spaces are different. Suppose that $\hat{e}_1$, $\hat{e}_2$, and $\hat{e}_3$ are mutually orthogonal unit vectors in the spin space and the spin quantization axis is $\hat{e}_3$. In such a case, the $\mathbf{d}$-vector is in the $\hat{e}_1$-$\hat{e}_2$ plane perpendicular to $\hat{e}_3$, and the relative angle between $\hat{e}_3$ and $\hat{p}_z$ is not yet determined.

For the ring geometry without the bias current, the $\mathbf{d}$-vector can be expressed with the use of two winding numbers m and n as

$$\mathbf{d} = \left[\frac{|\Delta_{\uparrow\uparrow}|}{\sqrt{2}}\hat{d}^{+}e^{-im\varphi} + \frac{|\Delta_{\downarrow\downarrow}|}{\sqrt{2}}\hat{d}^{-}e^{im\varphi}\right]e^{-in\varphi} \tag{18}$$

with $\hat{d}^{\pm} = \frac{1}{\sqrt{2}}(\hat{e}_1 \pm i\hat{e}_2)$. To grasp the physical meanings of m and n, it is convenient to consider the simplified case of $|\Delta| = |\Delta_{\uparrow\uparrow}| = |\Delta_{\downarrow\downarrow}|$ where Eq. (18) is reduced to $\mathbf{d} = |\Delta|e^{-in\varphi}[\hat{e}_1\cos(m\varphi) + \hat{e}_2\sin(m\varphi)]$. It is clear that n is the phase winding number, whereas m describes the rotation of the $\mathbf{d}$-vector along the circumference of the ring. In the case of $m = 0$, the $\mathbf{d}$-vector is spatially uniform and n takes an integer value such that the gap function can be single-valued. For $m \neq 0$, on the other hand, n and m can take half-integer values as well as integer values. This is because the gap function can also be single-valued with the half-integer values for n and m. This half-integer state accompanied with the $\mathbf{d}$-vector rotation corresponds to the so-called half-quantum vortex which has often been discussed in the context of superfluid ^{3}He [S38].

In the presence of the bias current [see Fig. S18a], the upper and lower arms of the ring are not equivalent. In other words, their winding numbers do not have to take the same values. Thus, the $\mathbf{d}$-vector can be expressed as:

$$d_\mu = \begin{cases} \left[\frac{|\Delta_{\uparrow\uparrow}|}{\sqrt{2}}\hat{d}_\mu^{+}e^{-im_1\varphi} + \frac{|\Delta_{\downarrow\downarrow}|}{\sqrt{2}}\hat{d}_\mu^{-}e^{im_1\varphi}\right]e^{-in_1\varphi} & (0 \leq \varphi \leq \pi) \\ \left[\frac{|\Delta_{\uparrow\uparrow}|}{\sqrt{2}}\hat{d}_\mu^{+}e^{-im_2\varphi} + \frac{|\Delta_{\downarrow\downarrow}|}{\sqrt{2}}\hat{d}_\mu^{-}e^{im_2\varphi}\right]e^{-in_2\varphi} & (\pi \leq \varphi \leq 2\pi) \end{cases}, \tag{19}$$

where the phase winding numbers n_1 and n_2 and the $\mathbf{d}$-vector ones m_1 and m_2 must satisfy the constraint shown in Table III, to avoid the phase mismatch at the intersections of the two arms[S6]. As shown in Fig. S18b, the constraint yields complicated $\mathbf{d}$-vector textures, except for the trivial case of $m_1 = m_2 = 0$ (type-I state) where the $\mathbf{d}$-vector is spatially uniform.

Table III| Constraint on the phase winding numbers n_1 and n_2 and the $\mathbf{d}$-vector winding numbers m_1 and m_2. Examples of the $\mathbf{d}$-vector textures for type I, II, and III states are shown in Fig. S18b.

Type	n_1, n_2	m_1, m_2	$n_1 - n_2$	$m_1 - m_2$
I	integer	$m_1 = m_2 = 0$	even	0
II	integer	integer $\neq 0$	even odd	even odd
III	half integer	half integer	even odd	even odd

Now, we consider the relative angle between the spin polarization direction $\hat{e}_3$ and the $\hat{p}_z$ direction corresponding to the ring axis. In the LP experiment where the magnetic field $\mathbf{H}$ is applied along the ring axis parallel to $\hat{p}_z$, the relation $\hat{e}_3 \parallel \mathbf{H} \parallel \hat{p}_z$ is satisfied. In the Bi/Ni system, however, there exists an in-plane stray field $\mathbf{H}_\mathrm{M}$ stemming from the Ni layer. Thus, the spin polarization direction $\hat{e}_3$, which corresponds to the $\mathbf{H}+\mathbf{H}_\mathrm{M}$ direction, should be tilted from the ring axis, i.e., from the $\hat{p}_z$ direction, by an angle θ_H. The angle θ_H connecting the spin and momentum spaces is included in the GL free energy via the $\delta f_\mathrm{D}^{(2)}$ term. The contribution to the free energy density can be calculated as

$$\frac{\lambda_D}{2}\left\{\left(\frac{1}{3}-\frac{1}{2}\sin^2\theta_\mathrm{H}\right)(|\Delta_{\uparrow\uparrow}|^2+|\Delta_{\downarrow\downarrow}|^2)-\gamma\sin^2\theta_\mathrm{H}|\Delta_{\uparrow\uparrow}||\Delta_{\downarrow\downarrow}|\right\} \tag{20}$$

with

$$\gamma=\begin{cases} 1 & (m_1=m_2=0) \\ \frac{1}{2} & (m_1=0 \ \text{or} \ m_2=0) \\ 0 & (m_1,m_2;\text{integer}\neq 0) \\ \frac{1}{2\pi}\left(\frac{1}{m_1}-\frac{1}{m_2}\right) & (m_1,m_2;\text{half integer}) \end{cases}, \tag{21}$$

where the above result is obtained by substituting $A_{\mu,i}=d_\mu w_{\mathbf{p},i}$ with $w_{\mathbf{p},i}=\frac{1}{\sqrt{2}}(\hat{p}_x+i\hat{p}_y)_i$ and Eq. (19) into Eq. (15), and also by performing some straightforward manipulations[S40]. One can see from the coefficient shown in Eq. (21) that the energy gain due to the $\delta f_\mathrm{D}^{(2)}$ term depends on the combination of m_1 and m_2 [see Eq. (21)], i.e., the $\mathbf{d}$-vector configuration. Such an energy difference proportional to γ [see the last term in Eq. (20)] is active only when $\theta_\mathrm{H}\neq 0$, i.e., the in-plane stray field is present as is actually the case for the Bi/Ni system.

In the same manner as that for Eq. (20), one can calculate the total free energy density. The GL equations $\frac{\delta f_\mathrm{GL}}{\delta|\Delta_{\uparrow\uparrow}|}=0$ and $\frac{\delta f_\mathrm{GL}}{\delta|\Delta_{\downarrow\downarrow}|}=0$ yield

$$\begin{aligned}|\Delta_{\sigma\sigma}|^2=-\frac{1}{4\beta_0}\Bigg\{&\frac{\alpha-\epsilon_\sigma\delta\alpha}{3}+\frac{K'}{R^2}\left[\left(n_1+\epsilon_\sigma m_1-\frac{\Phi}{\Phi_0}\right)^2+\left(n_2+\epsilon_\sigma m_2-\frac{\Phi}{\Phi_0}\right)^2\right] \\ &+\lambda_D\left[\frac{1}{3}-\frac{1}{2}\sin^2\theta_\mathrm{H}-\frac{1}{2}\gamma\sin^2\theta_\mathrm{H}\frac{|\Delta_{-\sigma-\sigma}|}{|\Delta_{\sigma\sigma}|}\right]\Bigg\}.\end{aligned} \tag{22}$$

Here, $\epsilon_{\uparrow(\downarrow)}=1(-1)$, $\Phi=\pi R^2 H$ is the magnetic flux passing through the ring of radius R, and Φ_0 is the flux quantum. By substituting $A_{\mu,i}=d_\mu w_{\mathbf{p},i}$ into Eq. (16), the total current density $\mathbf{j}_\mathrm{tot}$, which is sum of the superconducting current densities flowing in the upper and lower arms of the ring, is calculated as

$$\mathbf{j}_\mathrm{tot}=-\hat{\varphi}\frac{4|e|N(0)K'}{R}[(|\Delta_{\uparrow\uparrow}|^2+|\Delta_{\downarrow\downarrow}|^2)(n_1+n_2)+(|\Delta_{\uparrow\uparrow}|^2-|\Delta_{\downarrow\downarrow}|^2)(m_1-m_2)], \tag{23}$$

where $|\Delta_{\uparrow\uparrow}|$ and $|\Delta_{\downarrow\downarrow}|$ are the solutions of Eq. (22). The maximum value of $|\mathbf{j}_{\rm tot}|$ as a function of n_1, n_2, m_1, and m_2 under the constraints shown in Table III corresponds to $j_{\rm c}$. In this work, the obtained $j_{\rm c}$ is normalized by $j_0 = N(0)T_{\rm c0}|e|v_{\rm F}$.

Figure S18c shows the LP oscillation in $j_{\rm c}$ in the absence of the spin-orbit interaction of dipole type ($\lambda_{\rm D} = 0$). At each field, the highest critical current density among $j_{\rm c}$'s for various combinations of m_1 and m_2 gives a physical critical current density. As reported in Ref. S6, in the low-field region, the type-I state (green curve) with the spatially uniform **d**-vector is stable, whereas in the high-field region, the type-II and type-III states (bluish and reddish curves) having the complicated **d**-vector textures are realized. The physical $j_{\rm c}$ exhibits the conventional LP oscillation irrespective of whether the most stable superconducting state is type I, II, or III. Although the half-quantum-shifted oscillation is potentially possible (for example, see the red curve), it is energetically unstable except for some degenerate points (compare the red and blue curves).

In the presence of the spin-orbit coupling ($\lambda_{\rm D} \neq 0$), on the other hand, the half-quantum-shifted LP oscillation can be realized simply due to the energetics. Remember that the energy gain due to the spin-orbit coupling depends on the combinations of m_1 and m_2 [see Eq. (21)]. As one can see from Fig. S18d, with increasing the tilting angle $\theta_{\rm H}$, $j_{\rm c}$ for the type-III state with $m_1 = \frac{1}{2}$ and $m_2 = -\frac{3}{2}$ (red curve) is gradually elevated and eventually overwhelm $j_{\rm c}$ for the originally stable type-II state with $m_1 = 1$ and $m_2 = -1$ (blue curve). As a result, in the case of $\lambda_{\rm D} = 0.005$ and $\theta_{\rm H} = 30°$ [see the left panel of Fig. S18d], the physical $j_{\rm c}$ shows the conventional behavior in the low-field region of $\Phi/\Phi_0 < 10$, while in the high-field range of $10 < \Phi/\Phi_0 < 18$, it shows the half-quantum-shifted LP oscillation. Such a field-induced half-quantum shift of the LP oscillation is consistent with the experimental observation in the Bi/Ni superconducting ring.

Here, we comment on additional effects which are not incorporated in the above calculations. Although the tilting angle $\theta_{\rm H}$ gradually changes with increasing the magnetic field, we have used constant values of $\theta_{\rm H}$ in the above field-sweep calculation. As our focus is on the higher-field region where the usual and half-quantum-shifted LP oscillations are competing, such a constant-value approximation would be reasonable in this field range, as long as the in-plane stray field $\mathbf{H}_{\rm M}$ is not so large compared with the applied field $\mathbf{H}$. As mentioned in Sec. 5, the Meissner effect for the Bi/Ni bilayer was observed even at 0 mT [see Ref. S9]. In addition, the magnetization at 0 mT depends on the magnetization direction of the Ni layer. These facts indicate that there exists an in-plane stray filed from the Ni layer even below $T_{\rm c}$ and the magnitude of the stray field can be estimated to be ~1 mT. This should work as $\mathbf{H}_{\rm M}$ in the Bi/Ni bilayer. In the field range of $\mathbf{H}_{\rm M} < \mathbf{H}$, $\theta_{\rm H}$ should be small. In such a case, the stability of the half-quantum-shifted LP oscillation depends on how large the spin-orbit coupling $\lambda_{\rm D}$ is. In the present work, we have introduced the dipole interaction as a spin-orbit coupling simply from the analogy to superfluid ^{3}He, the well-established example of the spin-triplet Cooper pairing. In the real Bi/Ni system, however, a different kind of spin-orbit interaction might play a similar role to that of the dipole interaction.

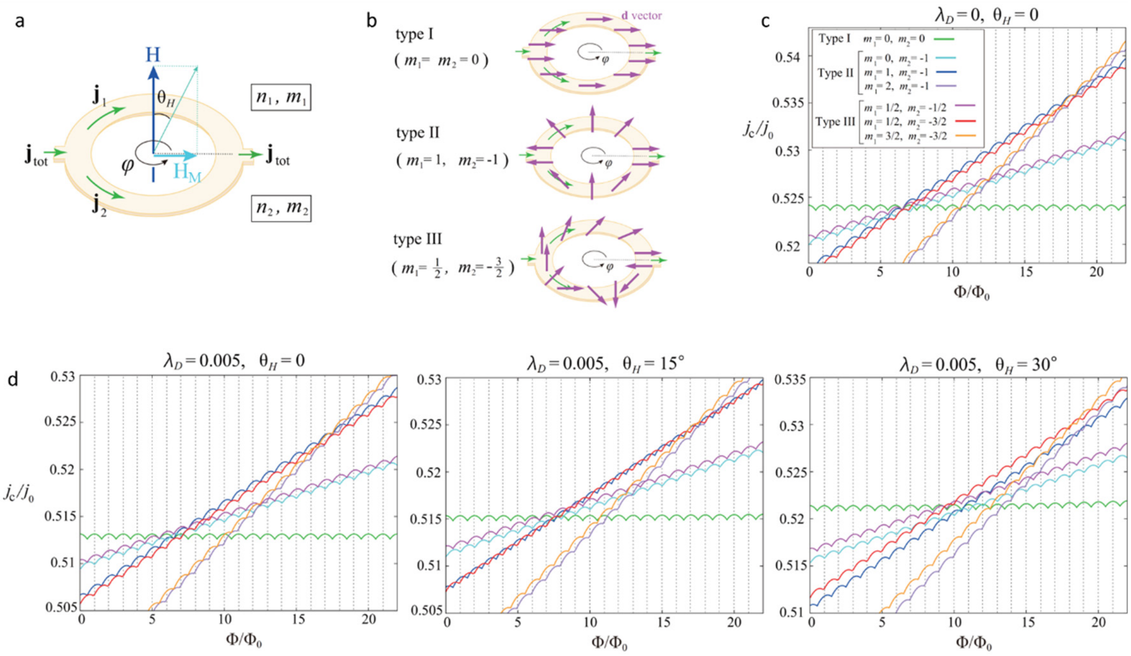

Fig. S18| System setup and the LP oscillation in the critical bias current density j_c. (a) A superconducting ring in the presence of an external magnetic field $\mathbf{H}$, a uniform in-plane stray field $\mathbf{H}_\mathrm{M}$, and a bias current density $\mathbf{j}_\mathrm{tot} = \mathbf{j}_1 + \mathbf{j}_2$, where φ denotes an azimuthal angle and θ_H denotes the tilting angle of $\mathbf{H} + \mathbf{H}_\mathrm{M}$ from the ring axis. n_1 and n_2 (m_1 and m_2) are the phase (**d**-vector) winding numbers in the upper and lower arms of the ring, respectively. (**b**) Schematically drawn **d**-vector textures in the type I, II, and III states in Table III, where a magenta arrow represents the **d**-vector and $|\Delta_{\uparrow\uparrow}| = |\Delta_{\downarrow\downarrow}|$ is assumed for ease of understanding. (**c**), (**d**) LP oscillations in j_c obtained at $T/T_{c0} = 0.7$ for the spin-triplet p-wave ring with $R/\xi_0 = 50$ and $\eta = 0.005$ in the cases (**c**) without and (**d**) with the spin-orbit coupling proportional to $\lambda_\mathrm{D} = 0.005$, where the color notations in (**d**) are the same as those in (**c**). In (**d**), the tilting angle θ_H is changed from $0°$ to $30°$ (from left to right).

References

S1. Gong, X. –X., Zhou, H. –X., Xu, P. –C., Yue, D., Zhu, K., Jin, X. –F., Tian, H., Zhao, G. –J. & Chen. T. –Y. Possible p-Wave Superconductivity in Epitaxial Bi/Ni Bilayers. *Chin. Phys. Lett.* **32**, 067402 (2015).

S2. Tokuda, M., Kabeya, N., Iwashita, K., Taniguchi, H., Arakawa, T., Yue, D., Gong, X., Jin, X., Kobayashi, K. & Niimi, Y. Spin transport measurements in metallic Bi/Ni nanowires. *Appl. Phys. Express* **12**, 053005 (2019).

S3. Yang, F. Y., Liu, K., Hong, K., Reich, D. H., Searson, P. C. & Chien, C. L. Large Magnetoresistance of Electrodeposited Single-Crystal Bismuth Thin Films. *Science* **284**, 1335 (1999).

S4. Lavine, J. M. Extraordinary Hall-Effect Measurements on Ni, Some Ni Alloys, and Ferrites. *Phys. Rev* **123**, 1273 (1961).

S5. Tinkham, M. Introduction to Superconductivity (Dover Publications, New York, 2004).

S6. Aoyama, K. Little-Parks oscillation and d-vector texture in spin-triplet superconducting rings with bias current. *Phys. Rev. B* **106**, L060502 (2022).

S7. Li, Y., Xu, X., Lee, M. –H., Chu, M. –W. & Chien, C. L. Observation of half-quantum flux in the unconventional superconductor β-Bi2Pd. *Science* **366**, 238-241 (2019).

S8. Tokuda, M., Nakamura, R., Maeda, M. & Niimi, Y. Higher harmonic resistance oscillations in micro-bridge superconducting Nb ring. *Jpn. J. Appl. Phys.* **61**, 060908 (2022).

S9. Zhou, H., Gong, X. & Jin, X., Magnetic properties of superconducting Bi/Ni bilayers. *J. Mag. Mag. Mater.* **422**, 73-76 (2017).

S10. Sivakov, A. G., Glukhov, A. M., Omelyanchouk, A. N., Koval, Y., Müller, P. & Ustinov, A. V. Josephson Behavior of Phase-Slip Lines in Wide Superconducting Strips. *Phys. Rev. Lett.* **91**, 267001 (2003).

S11. Kim, J., Doh, Y. J., & Lee, H. J. Quasiparticle-pair interference effect in proximity-coupled junction ladders. *Phys. Rev. B* **52**, 15095 (1995).

S12. Wel, J., Cadden-Zimansky, P. & Chandrasekhar, V. Observation of large $h/2e$ and $h/4e$ oscillations in a proximity dc superconducting quantum interference device. *Appl. Phys. Lett.* **92**, 102502 (2008).

S13. Petrashov, V. T., Antonov, V. N., Delsing, P. & Claeson, R. Phase memory effects in mesoscopic rings with superconducting ''mirrors''. *Phys. Rev. Lett.* **70**, 347 (1993).

S14. Petrashov, V. T., Antonov, V. N., Delsing, P. & Claeson, T. Non-linear phase memory effects in mesoscopic rings with superconducting "mirrors". *Physica B* **194–196**, 1105 (1994).

S15. Gong, X., Kargarian, M., Stern, A., Yue, D., Zhou, H., Jin, X., Galitski, V. M., Yakovenko, V. M. & Xia, J. Time-reversal symmetry-breaking superconductivity in epitaxial bismuth/nickel bilayers. *Sci. Adv.* **3**, e1602579 (2017).

S16. Ghadimi, R., Kargarian, M. & Jafari, S. A. Gap-filling state induced by disorder and Zeeman coupling in the nodeless chiral superconducting Bi/Ni bilayer system. *Phys. Rev. B* **100**, 024502 (2019).

S17. Chao, S. P. Superconductivity in a Bi/Ni bilayer. *Phys. Rev. B* **99**, 064504 (2019).

S18. Yi, H., Hu, L.-H., Wang, Y., Xiao, R., Cai, J., Hickey, D. R., Dong, C., Zhao, Y.-F., Zhou, L.-J., Zhang, R., Richardella, A. R., Alem, N., Robinson, J. A., Chan, M. H. W., Xu, X., Samarth, N., Liu., C.-X. & Chang, C.-Z. *Nat. Matter.* **21**, 1366 (2022).

S19. Zhao, G. J., Gong, X. X., He, J. C., Gifford, J. A., Zhou, H. X., Chen, Y., Jin, X. F., Chien, C. L. & Chen, T. Y. Triplet p-wave superconductivity with ABM state in epitaxial Bi/Ni bilayers. *arXiv*: 1810. 10403.

S20. Vaughan, M., Satchell, N., Ali, M., Kinane, C. J., Stenning, G. B. G., Langridge, S. & Burnell, G. Origin of superconductivity at nickel-bismuth interfaces. *Phys. Rev. Research* **2**, 013270 (2020).

S21. He, Q. L., Liu, H., He, M., Lai, Y. H., He, H., Wang, G., Law, K. T., Lortz, R., Wang, J. & Sou, I. K. Two-dimensional superconductivity at the interface of a Bi_2Te_3/FeTe heterostructure. *Nat. Commun.* **5**, 4247 (2014).

S22. Guo, J. G., Chen, X., Jia, X. Y., Zhang, Q. H., Liu, N., Lei, H. C., Li, S. Y., Gu, L., Jin, S. F. & Chen, X. L. Quasi-two-dimensional superconductivity from dimerization of atomically ordered $AuTe_2Se_{4/3}$ cubes. *Nat. Commun.* **8**, 871 (2017).

S23. Chun, C. S. L., Zheng, G. G., Vincent, J. L. & Schuller, I. K. Dimensional crossover in superlattice superconductors. *Phys. Rev. B* **29**, 4915 (1984).

S24. Kozuka, Y., Kim, M., Bell, C., Kim, B. G., Hikita, Y. & Hwang, H. Y. Two-dimensional normal-state quantum oscillations in a superconducting heterostructure. *Nature* **462**, 487 (2009).

S25. Deutscher, G. & Entin-Wohlman, O. Critical fields of weakly coupled superconductors. *Phys. Rev. B* **17**, 1249 (1978).

S26. Gong, X., Kargarian, M., Stern, A., Yue, D., Zhou, H., Jin, X., Galitski, V. M., Yakovenko, V. M. & Xia, J. Time-reversal symmetry-breaking superconductivity in epitaxial bismuth/nickel bilayers. *Sci. Adv.* **3**, e1602579 (2017).

S27. Chauhan, P., Mahmood, F., Yue, D., Xu, P. –C., Jin, X. & Armitage, N. P. Nodeless Bulk Superconductivity in the Time-Reversal Symmetry Breaking Bi/Ni Bilayer System. *Phys. Rev. Lett.* **122**, 017002 (2019).

S28. Tsuei, C. C., Kirtley, J. R., Chi, C. C., Yu-Jahnes, L. S., Gupta, A., Shaw, T., Sun, J. Z., &

Ketchen, M. B. Pairing Symmetry and Flux Quantization in a Tricrystal Superconducting Ring of $YBa_2Cu_3O_{7-\delta}$. *Phys. Rev. Lett.* **73**, 593 (1994).

S29. Mäkinen, J. T., Dmitriev, V. V., Nissinen, J., Rysti, J., Volovik, G. E., Yudin, A. N., Zhang, K., & Eltsov, V. B. Half-quantum vortices and walls bounded by strings in the polar-distorted phases of topological superfluid ^{3}He. *Nature Commun.* **10**, 237 (2019).

S30. Sato, M., Takahashi, Y., & Fujimoto, S., Non-Abelian topological orders and Majorana fermions in spin-singlet superconductors. *Phys. Rev. B* **82**, 134521 (2010).

S31. Agterberg, D. F. Magnetoelectric effects, helical phases, and FFLO phases, in Non-Centrosymmetric Superconductors: Introduction and Overview. eds. Bauer, E. & Sigrist, M. (Springer, Berlin, 2012).

S32. Fujimoto, S., & Yip, S. K. Aspects of spintronics, in Non-Centrosymmetric Superconductors: Intro-duction and Overview. eds. Bauer, E. & Sigrist, M. (Springer, Berlin, 2012).

S33. Mineev, V. P. & Samokhin, K. V. Nonuniform states in noncentrosymmetric superconductors: Derivation of Lifshitz invariants from microscopic theory. *Phys. Rev. B* **78**, 144503 (2008).

S34. Agterberg, D. F. & Tsunetsugu, H. Dislocations and vortices in pair-density-wave superconductors. *Nat. Phys.* **4**, 639 (2008).

S35. Agterberg, D. F., Davis, J. S., Edkins, S. D., Fradkin, E., Van Harlingen, D. J., Kivelson, S. A., Lee, P. A., Radzihovsky, L., Tranquada, J. M. & Wang, Y. The Physics of Pair-Density Waves: Cuprate Superconductors and Beyond. *Annu. Rev. Condens. Matter Phys.* **11**, 231 (2020).

S36. Dimitrova, O. & Feigel'man, M.V., Theory of a two-dimensional superconductor with broken inversion symmetry. *Phys. Rev. B* **76**, 014522 (2007).

S37 Aoyama, K. & Sigrist, M. Model for Magnetic Flux Patterns Induced by the Influence of In-Plane Magnetic Fields on Spatially Inhomogeneous Superconducting Interfaces of $LaAlO_3$-$SrTiO_3$ Bilayers. *Phys. Rev. Lett.* **109**, 237007 (2012).

S38. Volhardt, D. & Wolfle, P. The superfluid Phase of Helium 3. (Taylor and Fransis, London, 1990).

S39. Vakaryuk, V. & Leggett, A. J. Spin Polarization of Half-Quantum Vortex in Systems with Equal Spin Pairing *Phys. Rev. Lett.* **103**, 057003 (2009).

S40. Aoyama, K. in preparation.